Materials Advances

ROYAL SOCIETY OF CHEMISTRY

PAPER

View Article Online
View Journal

Cite this: DOI: 10.1039/d5ma01317h

Immobilized, micro-patterned graphene nanoflake devices for high-throughput, uniform intracellular biomolecular delivery

Donia Dominic,[a] Rajdeep Ojha,[b] Moeto Nagai,[c] Srabani Kar[ad] and Tuhin Subhra Santra *[ae]

Developing a high-throughput, safe, and adaptable method for intracellular delivery remains a bottleneck hindering the translation of molecular therapeutics and genome engineering. Nano-sensitizing particle-activated photoporation results in highly efficient cell transfection, but the throughput is limited, and managing cytotoxicity associated with the internalization of nanoparticles remains a challenge. This study presents an immobilized, micropatterned reduced graphene oxide (rGO)-based scalable and biocompatible platform with an automated laser scanning interface for high-throughput photoporation-mediated intracellular delivery. The device comprised an ordered array of rGO islands of 10 μm diameter with an interisland spacing of 30 μm on a glass substrate of 2 cm × 2 cm dimensions. The device was aligned atop the seeded layer of cells, and a 1064-nm infrared nanosecond pulse laser (28 mJ cm^{-2}) was scanned, inducing photothermal bubbles near the cell membrane. These bubbles rapidly expanded and collapsed, causing cell membrane deformation, thereby enabling uniform delivery to ~5 × 10^5 cells within 15 seconds. This platform successfully delivered various biomolecules including small-molecule dyes, siRNA, plasmids, and large-sized enzymes across different cancer cell lines and human mesenchymal stem cells (hMSCs). The best results were achieved with an enzyme transfection efficacy of 94% and a cell viability of 99% in hMSCs. This method provides a scalable and versatile bio-interface approach, paving the way for high-throughput intracellular delivery for therapeutic, diagnostic, and regenerative medicine applications and innovations.

Received 12th November 2025,
Accepted 29th December 2025

DOI: 10.1039/d5ma01317h

rsc.li/materials-advances

1. Introduction

The efficient delivery of biomolecules, cellular organelles, and functional nanomaterials into cells without compromising their viability is a promising strategy that contributes substantially to biomedicine and bioengineering.[1,2] Among all the available intracellular delivery methods such as viral,[3,4] chemical[5,6] and physical,[7] the physical methods are desirable, as they bypass the uncontrollable endocytosis process and offer unlimited, diverse shape- and size-based cargo delivery without any cell specificity and toxicity.[8–11] Physical methods use physical stimuli such as mechanical,[12] electrical,[13,14] optical,[15] and sound waves[16] to create transient hydrophilic pores in the plasma membrane, through which biomolecules can be gently delivered into the cells before the pores are resealed.[8,17,18] Among different physical methods, the mechanoporation is a low-throughput, laborious process that requires highly skilled personnel. The electroporation, ultrasound waves, or sonoporation can cause irreversible cell damage and significantly reduce cell viability.[19] However, photoporation, which uses optical stimuli for transfecting cells, is a high-throughput intracellular delivery method that offers significant advantages.[19–22] The photoporation of cells by tuning light–matter interaction does not cause any permanent damage to the cells until a high laser fluence is applied. As a contactless process, it reduces the risk of contamination, yielding high cell viability.[15,23] In this method, the laser fluence and exposure time can be modulated to obtain high spatial and temporal selectivity, facilitating the transport of large-sized biomolecules into live cells while eliminating the risk of contamination.[11,17,24]

Photoporation using photosensitizing materials efficiently reduces the laser fluence requirement for cell transfection, as it leverages the plasmonic/photothermal effects of these materials to form transient cell membrane pores at low laser fluences. This approach offers a higher transfection efficiency with high cell viability.[25–27] Here, the cells are incubated with photosensitizer nanoparticles such as gold nanoparticles, reduced

[a] Department of Engineering Design, Indian Institute of Technology, Madras, India. E-mail: tuhin@smail.iitm.ac.in, santra.tuhin@gmail.com
[b] Department of Physical Medicine and Rehabilitation, Christian Medical College, India
[c] Department of Mechanical Engineering, Toyohashi University of Technology, Japan
[d] Department of Physics, Indian Institute of Technology, Hyderabad, India
[e] School of Interdisciplinary Studies, Indian Institute of Technology Madras, India

graphene oxide, and carbon nanoparticles. Upon laser illumination, the plasma membrane becomes permeable due to the thermal denaturation of glycoproteins in the phospholipid bilayer, resulting from the shock waves generated by the rupture of nanobubbles originating from the localized heating of nano-sensitizer particles.[21,26,28] It has been proven that the size of plasma membrane pores can be varied to deliver various sizes of biomolecules by adjusting the laser energy, exposure time, and shapes and sizes of photosensitized nanomaterials.[26,27,29,30] As local cell membrane permeabilization is caused by these photosensitizing nanomaterials, an unfocused, broad laser beam can be used instead of a tightly focused laser beam.[30]

Although the nanophotosensitizer-mediated photoporation method has several advantages, random adsorption of nanophotosensitizer particles on the cell membrane may reduce the uniformity of delivery, delivery efficiency, and reproducibility.[31] Furthermore, the uptake of nanoparticles into the cells can result in cytotoxicity, affecting cell viability and biosafety.[32,33] Tsoli *et al.* demonstrated that cellular uptake of Au55 nanoclusters resulted in DNA damage and cellular toxicity in both healthy and cancerous cells.[33] Luo *et al.* explained that the pre-incubation of iron oxide nanoparticles (IONPs) resulted in reduced cell viability, morphological degeneration, impaired mitochondrial function, and mild oxidative stress, which can increase the cytotoxicity effects of IONPs due to ferroptosis.[34] It has been shown that the immobilization of nanoparticles onto surfaces can eliminate the above-mentioned drawbacks.[21,35]

Over the last two decades, the rapid development of micro- and nano-fabrication technologies[10,36] combined with the integration of biology has led to frontier research in micro/nano device-based photoporation, which enhances delivery throughput, efficiency, and cell viability.[10,21] Many of the developed photoporation devices require cells to be cultured overnight on the devices before being subjected to laser exposure to increase the delivery efficiency and cell viability.[25,37–39] Lyu *et al.* cultured the cells on a device with a gold nanoparticle layer and exposed them to an 808 nm CW laser to achieve a plasmid transfection efficiency of $\approx$53% for mouse embryonic fibroblasts and $\approx$44% for human umbilical vein endothelial cells (HUVECs); however, the platform lacked control over the number of contact points between the gold layer and cells, which resulted in reduced transfection efficiency.[37] Zhao *et al.* fabricated a Au nano disk array coupled with a nanosecond pulse laser of fluence 110 mJ cm^{-2}, to achieve high transfection efficiencies of 98% for 0.6 kDa calcein and 94% for 4 kDa calcein in HeLa cells, but the transfection efficiency reduced drastically to 36% as the size of the biomolecule increased to 150 kDa dextran.[39] Due to a lack of control over the number of contact points between cells and the device, most reported device-based photoporation platforms lack uniform delivery and are incapable of transfecting large biomolecules across cell types with high transfection efficiency and cell viability. Additionally, most platforms require overnight cell culture on the device, which may affect the physiology of cells.

It is known that graphene and graphene-derived compounds are potential candidates for various applications due to their unique properties.[40] Their superior mechanical,[41] electrical,[42] thermal[43] and optical[44,45] characteristics combined with biocompatibility[46,47] make them promising in the field of bioengineering and biomedicine. The reduction of graphene oxide (GO) to form reduced graphene oxide (rGO) is a cost-effective method of producing graphene in bulk. Control over the degree of reduction helps in tuning different properties of graphene like surface area, electrical conductivity, thermal conductivity, and solubility.[48] When compared with conventionally used materials in photoporation platforms, reduced graphene oxide (rGO) offers significant advantages including lower production costs, scalability, reduced degradability, ease of micropatterning, and chemical tunability. Unlike the plasmonic nanoparticles such as gold and titanium, which show strong absorption at specific wavelengths, the broad and flat spectral characteristics of rGO range from the visible to the NIR region[49] along with its biocompatibility,[47] large specific surface area, and excellent photothermal properties,[50,51] making rGO a good candidate for use as a photosensitizer material for cellular therapy and diagnostics. In recent works,[52,53] Harshan Padma *et al.* introduced an rGO-mixed PDMS micro pyramid device[52] to generate cavitation and facilitate photoporation at an ultra-low fluence, achieving high delivery efficiencies and viabilities. Although the microtip geometry excels at light trapping and enables cavitation at a very low fluence, it requires the microfabrication of 3D pyramids, which involves steps such as photolithography and complex chemical etching. In contrast, in the rGO-mixed PDMS thin-sheet device,[53] heat distribution occurs randomly across dispersed rGO flakes within the PDMS sheet, complicating the regulation of individual cell exposure doses and leading to inconsistent delivery. Conversely, a micropatterned rGO platform offers precise spatial control over the size, density, and distribution of rGO islands, thereby ensuring uniform rGO and cell interfaces throughout the device and minimizing variability in delivery outcomes. Furthermore, intracellular delivery has been conducted in cancer cells and mouse cells; however, further research focused on stem cells is warranted.

Herein, we report a photoporation platform coupled with a simple and scalable micro-patterned rGO device with dimensions of 2 cm $\times$ 2 cm, comprising circular rGO islands with a diameter of 10 μm and an interisland spacing of 30 μm, fabricated on a glass coverslip, for the high-throughput delivery of different biomolecules to diverse cell types. The immobilization of rGO into predefined micropatterns helps maintain good cell viability by preventing nanoparticle entry into cells. In this device, heating is intentionally localized to lithographically defined rGO micropatterns, providing control over the number of contact points between cells and the device. Our platform uses a nanosecond pulse laser (5 ns pulse width, 10 Hz frequency) with a low laser fluence of 28 mJ cm^{-2} at an NIR wavelength of 1064 nm to achieve massively parallel high-throughput cell transfection. A motorized laser scanning stage facilitates adjusting the scanning area, thereby enhancing the

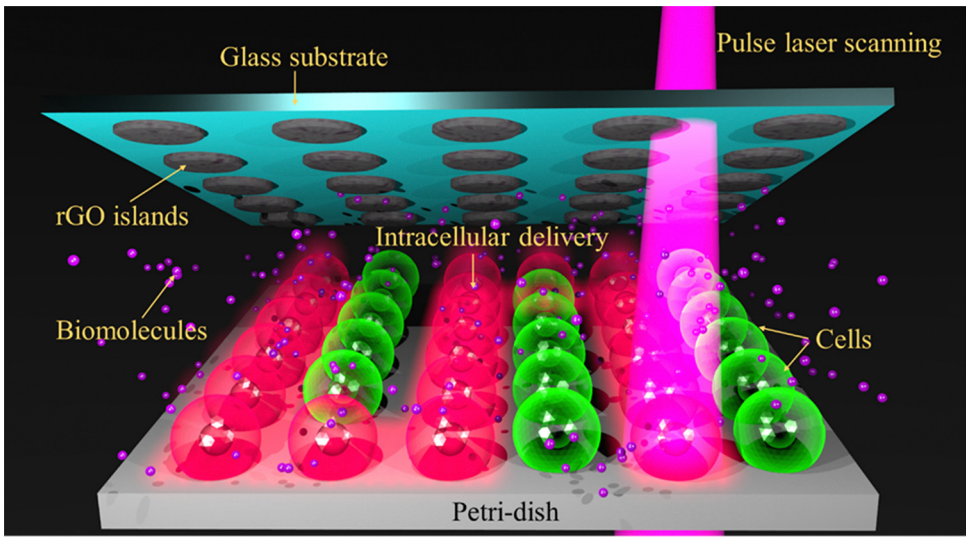

Fig. 1 Schematic of an array of rGO islands in the micro-patterned device that activated high-throughput intracellular biomolecular delivery. Upon pulse laser scanning on the top of the micro-patterned rGO device, transient pores are created in the cell membrane, facilitating the diffusion of biomolecules into the cells.

platform's scalability. Moreover, the scanning speed can be varied to control the laser exposure duration to facilitate high-throughput transfection of biomolecules. The schematic of the intracellular delivery platform for a monolayer of cells employing the rGO device is shown in Fig. 1. By combining the advantages of light-activated photoporation with the exceptional photothermal properties and biocompatibility of rGO, we successfully transfect different-sized biomolecules into various mammalian cell lines including hMSCs, with high transfection efficiency while maintaining high cell viability.

2. Materials and methods

2.1 Chemicals

Graphite fine powder (98%), hydrogen peroxide solution (30%; Loba Chemie Pvt. Ltd, India), potassium permanganate, sulphuric acid (98%), *ortho*-phosphoric acid (85%), and hydrochloric acid (35%) (Merck Life Science Private Limited, India) were used for rGO synthesis. All chemicals obtained from the indicated sources were used as received without further purification, and all were of reagent grade.

2.2 Bioreagents

Calcein acetomethoxy fluorescein complex (Calcein AM, 1 mg mL^{-1}, Invitrogen, excitation/emission maxima, 495/515 nm) and calcein red-orange AM (calcein red-orange AM, 1 mg mL^{-1}, Invitrogen, excitation/emission maxima, 577/590 nm) were used to test cell viability after photoporation. Hoechst 33342 (Invitrogen) was used for cell nucleus staining. Four different types of impermeable biomolecules with different sizes were used to validate the transfection efficiency of our platform. Propidium iodide (PI) red-fluorescent nuclear and chromosome counterstain was procured from Invitrogen. A universal negative control siRNA (MISSION® siRNA Fluorescent Universal Negative Control #1, 6-FAM) was procured from Sigma-Aldrich. The plasmids were extracted from 250 mL cultures using the HiPurA Silica Kit (HiMedia). Restriction digestion was used to confirm the EGFP plasmids' authenticity and integrity, and 0.8% agarose gel was used to resolve the restricted fragments. The enzyme β-galactosidase derived from *Escherichia coli* (β-galactosidase, G5635) was purchased from Sigma-Aldrich. Other cell culture reagents used were Dulbecco's modified Eagle medium (DMEM, Gibco), minimum essential medium α (MEM α, Gibco), fetal bovine serum (FBS, Gibco), penicillin–streptomycin (PS, Invitrogen), MEM (minimum essential medium) non-essential amino acids (MEM NEAA, Gibco), 0.25% trypsin–EDTA (1×) (Thermo), and phosphate buffer saline (10× PBS, Himedia).

2.3 Synthesis of reduced graphene oxide (rGO)

The initial material chosen for the synthesis of reduced graphene oxide (rGO) was graphite. The required graphene oxide (GO) for the experiment was synthesized from graphite using the Tour method or improved method.[54,55] It is one of the most efficient methods for producing hydrophilic GO. This utilizes potassium permanganate as an oxidizing agent under acidic conditions to synthesize GO. For this, 0.5 g of graphite powder was introduced to a 9 : 1 mixture of H_2SO_4 and H_3PO_4, and then it was sonicated for 3 hours to enhance the intercalation and efficiency of the oxidation process. To the above-mentioned mixture, 3 g of $KMnO_4$ was added under constant stirring at 300 rpm. For the next 24 hours, the reaction mixture was kept under stirring, maintaining the temperature below 50 °C, and the reaction mixture turned thick and brown. After sonication for 90 minutes to reduce the particle size, we added 250 mL of DI water under stirring conditions, which produced a large exotherm. Further, 30% H_2O_2 was slowly added till the solution turned bright yellow. The addition of H_2O_2 helps in the removal

of residual permanganate and manganese dioxide. The solution was allowed to settle, the supernatant was removed, and the residual solution was washed with HCl, ethanol, and water, respectively (2× times), till the pH of the solution stabilized at neutrality.

The collected residue was dried in an oven at 50 °C for 48 hours to obtain a graphene oxide powder. This method provided a greater amount of GO materials as compared to Hummers' method[56] or modified Hummers' method.[57] The reduction of GO to rGO helps in restoring the graphitic structure and improves the photothermal properties.[58,59] Most of the oxygen-containing groups on the surface of GO were removed during the reduction process to produce rGO. The green reduction of graphene oxide is achieved by the irradiation of graphene oxide with a high-power ultraviolet light source (253 nm, 130 W, Arklite Speciality Lamps Pvt. Ltd).[60]

2.4 Characterization techniques

Transmission electron microscopy (TEM, JEOL 1400 operating at 120 kV) imaging was employed to examine the geometry and structural morphology of rGO nanosheets. The confocal-Raman spectroscopy (WiTEC R 300 source: Nd-YAG, 532 nm-457 nm range: 100–3600 1 cm^{-1}) and Fourier transform infrared (FTIR) spectroscopy (Bruker-Alpha-Platinum, 500–4000 cm^{-1}) were used for understanding the molecular composition and structural details of the synthesized rGO and micropatterned rGO device. The UV-vis spectroscopy (PerkinElmer UV WinLab 6.4.0.973/2.02.06 Lambda 900 UV/VIS/NIR) analysis was performed to examine the absorption spectrum of the rGO nanosheets. The characterization results of synthesized rGO are shown in Fig. 2. Scanning electron microscopy (SEM, Verios G4 UC HRSEM) was employed to analyze the structural morphology and pattern fidelity of the fabricated micro-patterned rGO device.

2.5 rGO micro-array device design and fabrication

The proposed design of the micro-patterned rGO device (2 cm × 2 cm) includes an array of 10 μm circular rGO islands on a glass substrate, with an inter-island spacing of 30 μm. The size of each rGO island and the distance between islands are the two primary criteria that affect the device performance. To achieve uniform, high-throughput biomolecular transfection on a monolayer of cells, these parameters were selected, taking into account fabrication constraints and experimental requirements.

For fabrication, a glass coverslip measuring 2.2 cm × 2.2 cm was used as the device substrate. The coverslip was initially cleaned with a Piranha solution, containing a 7 : 1 mixture of sulphuric acid (H_2SO_4) and hydrogen peroxide (H_2O_2) and maintained at 80 °C for 20 minutes. This was followed by

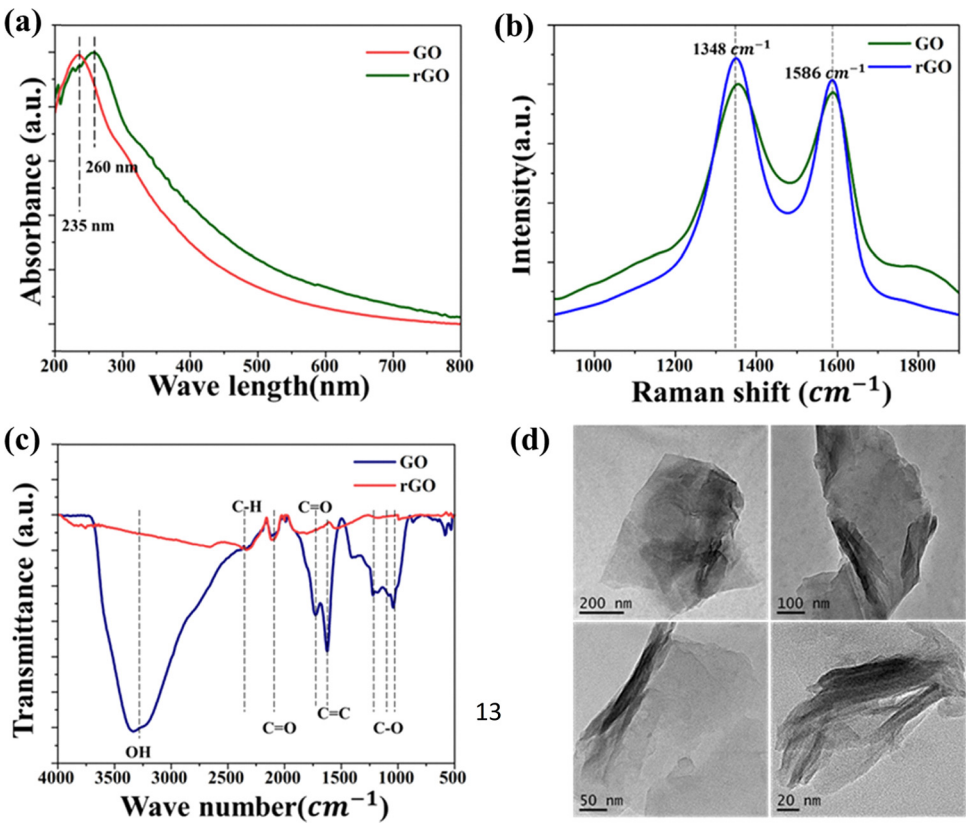

Fig. 2 Characterization of GO and rGO nanosheets. (a) UV-Vis spectra with maximum absorbance of GO at 235 nm and that of rGO at 260 nm. (b) Raman spectra with the corresponding D band at 1348 cm^{-1} and G band at 1586 cm^{-1}. (c) Fourier-transform infrared (FTIR) spectra with C–H, C═O, C═C, C–O, and O–H stretching. (d) Transmission electron microscopy (TEM) images of rGO nanosheets with a thickness of few to several layers.

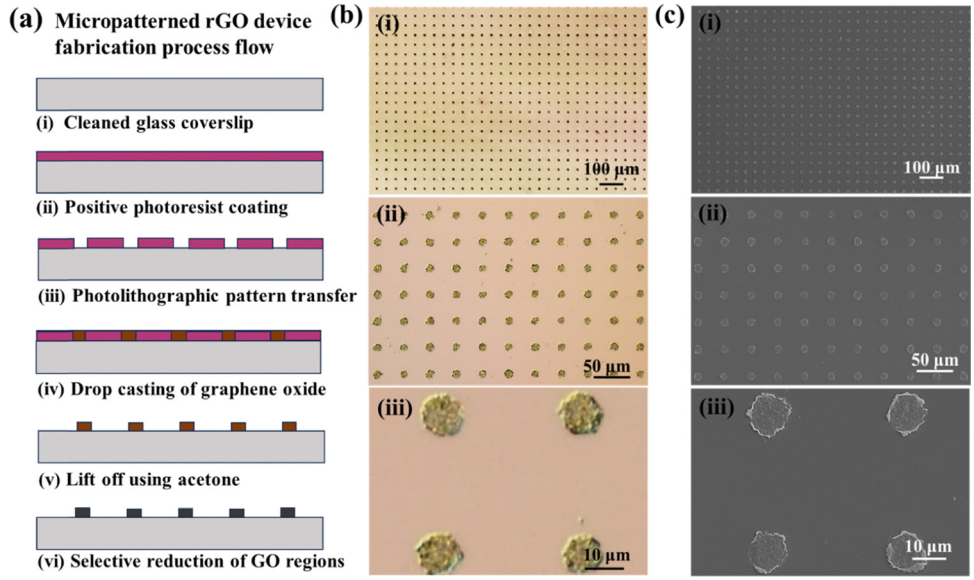

Fig. 3 The micro-patterned rGO device with an array of 10 μm-diameter rGO islands and an inter-island spacing of 30 μm fabricated on a glass coverslip. (a) Illustration of the process steps (i)–(vi) involved in fabricating the micropatterned rGO device. (b) Optical images of the rGO device (i)–(iii) at different magnifications and (c) SEM images of the micro-patterned rGO device (i)–(iii) at different magnifications, revealing the surface morphology of the device.

thorough cleaning with deionized water (10 minutes), acetone (3 minutes), and isopropanol (IPA) (3 minutes). The coverslip was subsequently dried using a nitrogen blow. Before photolithographic patterning, it was prebaked at 110 °C for 2 minutes to eliminate any residual moisture and then cooled to room temperature. An illustration of the steps involved in the fabrication of the micropatterned reduced graphene oxide (rGO) device is shown in Fig. 3(a). The coverslip was spin-coated with positive photoresist AZ5214E for 5 seconds at 500 rpm, followed by 30 seconds at 3500 rpm, and then soft-baked at 110 °C for 1 minute to facilitate solvent evaporation. Subsequently, UV photolithography was performed using the designed positive photomask to transfer the pattern. The UV-exposed regions of the photoresist were removed using an AZ 400 K developer.

After photolithographic patterning, 1 mL of GO solution (0.125 mg mL^{-1}) was drop-cast onto the photoresist-patterned coverslip and dried in an oven at 50 °C for 1 hour. The rectangular array of circular GO micropatterns was obtained after lifting off the unwanted photoresist areas by sonicating in acetone for 30 seconds, followed by an IPA (isopropyl alcohol) wash. Finally, the circular GO islands were selectively reduced to rGO islands by exposing the patterned area to high-power UV light for 2 hours. Using the above-mentioned method, an array of circular rGO islands with a diameter of 10 μm and inter-island spacings of 30 μm, 40 μm, 50 μm, and 60 μm were fabricated.

2.6 Cell culture

For the experiment, human cervical carcinoma (SiHa) cells, human glioblastoma (LN-229) cells, and mouse fibroblast (L929) cells were obtained from the National Centre for Cell Science (NCCS) in Pune, India. Human mesenchymal stem cells (hMSCs) were acquired from Lonza, USA. Before starting the experiments, the cell lines (L929, SiHa, and LN-229) were cultured in tissue culture flasks using Dulbecco's modified Eagle medium (DMEM, Gibco), while hMSCs were cultured in minimum essential medium α (MEM α, Gibco), supplemented with 10% FBS, 1% penicillin–streptomycin (PS, Invitrogen), and 1% MEM Non-Essential Amino Acids (MEM NEAA, Gibco). All cells were maintained in a humidified incubator with 5% CO_2 at 37 °C.

2.7 Intracellular biomolecular delivery experimental procedure

The cells were cultured overnight in a 35 mm Petri dish at a concentration of 2.5×10^5 cells per mL. Once the cells adhered to the dish, the old media were removed, and the cells were rinsed with 1× phosphate-buffered saline (PBS) to eliminate dead cells and debris. Subsequently, Dulbecco's modified Eagle medium (DMEM), supplemented with the required biomolecules, was added and incubated for approximately 4–5 minutes. Finally, the micro-patterned rGO device was inverted and placed on top of the monolayer of cells, bringing the device surface into close contact with the cell layer.

After the rGO device was aligned, an infrared (1064 nm) nanosecond pulse laser (EKSPLA, NT-342B-10-AW10, Lithuania, with a pulse width of 5 ns, a frequency of 10 Hz, and a focal spot size of 6 mm) was scanned over the rGO device using a motorized scanning stage. Upon laser exposure, the rGO nanosheets induced heat and generated photothermal bubbles, which rapidly expanded and collapsed, resulting in strong fluid flow near the cell membrane. Consequently, the cell membrane formed permeable pores, allowing biomolecules to be gently delivered into cells through a simple diffusion process.[29,61,62]

The membrane resealed over time once laser irradiation was ceased. The resealing time depends on the laser fluence, shape, and size of the micro/nanostructured materials, as well as the exposure time. To attain uniform delivery, every cell must make contact with the photosensitizer area (rGO island), and the number of contact points per cell should be uniform throughout the cell layer. With the increase in interspacing, some cells may not have a point of contact with the rGO island, resulting in non-uniform delivery. However, reducing the interspacing will cause cells to come in contact with more rGO islands, which may decrease cell viability due to the overheating of rGO resulting from pulse-laser interaction. By merging the images of a monolayer of cells and micro-patterned rGO device, we found that at an inter-island spacing of 30 μm, each of the cells will be in contact with one rGO island. Reducing the inter-island spacing will result in more contact points per cell, while increasing the inter-island spacing will leave the cell without any contact points. The bright-field merged images of the rGO device and a monolayer of cells are shown in Fig. S1 of the SI.

Propidium iodide (PI, 668 Da, at a working concentration of 50 μg mL^{-1}) was used as a model dye to optimize the laser parameters including laser fluence, exposure time, and laser scanning speed, for successful intracellular delivery. The PI dye is cell-impermeable and typically stains only cells with compromised membranes, such as dead or membrane-porated cells.[55,56] During photoporation, the cell membrane becomes permeabilized because of the acoustic pressure generated by the rupture of photothermal bubbles, allowing PI to diffuse into the cell and produce red fluorescence in the live cell cytosol. Initial experiments were conducted on a monolayer of LN-229 cells on a 35 mm Petri dish. Since the PI dye can stain dead cell nuclei, Calcein AM dye was used to label viable cells. Calcein AM is a non-fluorescent, hydrophobic, lipophilic dye that is hydrolyzed by intercellular esterase, releasing highly fluorescent, hydrophilic, cell-impermeable Calcein, which gives bright green fluorescence to the live cell cytosol.[10] To successfully deliver various-sized biomolecules into different cell lines, either the scanning speed or the laser fluence must be adjusted. In this study, the fluence was kept constant. At the same time, the scanning speed was varied to control the laser exposure time, thereby enabling highly efficient delivery of different-sized biomolecules into cells with high cell viability.

After optimizing and successfully delivering the PI dye, we attempted to deliver siRNA. The siRNA is an RNA molecule that silences the targeted gene or prevents its expression. This is performed by cleaving the mRNA encoding the targeted gene. The siRNAs are generally used for therapeutic applications to knock down disease-related genes.[63] Here we employed a universal negative control siRNA, which was conjugated with 6-FAM (MISSION® siRNA Fluorescent Universal Negative Control #1, 6-FAM, Sigma Aldrich). This siRNA is 20–24 bp long, and is generally used to study transfection efficiency, as its expression can be easily visualized.[64] The siRNA, tagged with 6-FAM, will cause the cells to exhibit green fluorescence once it is delivered into the live cells, even though it has no gene-silencing properties. For experiments, we used a final siRNA concentration of 2 μM and an incubation time of 15 minutes. For each set of experiments, the laser exposure duration was gradually increased by reducing the scanning speed from 15 mm s^{-1}. The fluorescence images for all siRNA experiments were captured 24 hours after siRNA transfection, because it takes 8–24 hours for the siRNA expression.[10,11]

Next, to assess EGFP expression, we examined the delivery of a plasmid DNA coding for EGFP (EGFP-pcDNA) (6159 bp). Once the gene coding for EGFP enters the cell, it will be transcribed and translated to produce GFP, the expression of which can be visualized by green fluorescence.[65] We used an optimized concentration of 125 μg mL^{-1}, and the laser scanning speed was set to 7 mm s^{-1} to achieve the best EGFP expression. A longer exposure time is needed to successfully transfect an EGFP plasmid due to the larger size of the biomolecule than that used in our previous experiments. After transfection, plasmid DNA encoding EGFP takes about 12–24 hours to express the gene and produce a green fluorescence signal. Therefore, the images were taken 24 hours after transfection, and Calcein red-orange AM was used to stain the live cells following photoporation experiments.

Furthermore, we utilized β-galactosidase enzyme (465 kDa) as a functional biomolecule for delivery. Intracellular delivery of the β-galactosidase enzyme will help assess the ability of our photoporation platform to deliver large therapeutic proteins into cells. The β-galactosidase enzyme is an exoglycosidase that catalyzes the cleavage of β-galactosidic bonds in disaccharides, breaking lactose into glucose and galactose.[10] This enzyme, tagged with a specific protein, is typically used as a reporter enzyme to indicate gene expression. For our experiments, we used β-galactosidase enzyme derived from *E. coli* (Sigma Aldrich) and conjugated it with a fluorescent molecule (Cy5; 1 mg mL^{-1}; Sigma Aldrich) for easy visualization. With a final enzyme concentration of 22.5 U mL^{-1}, the optimized reduced scanning speed was 5 mm s^{-1}, resulting in successful intracellular transfection of enzymes into cells. The decrease in laser scanning speed is due to the need for a longer exposure time on the cell membrane to generate large pores, which helps larger biomolecules enter the cells. Once the β-galactosidase enzyme is successfully delivered into the cell, the cells will produce red fluorescence because of the Cy5 conjugation. Since the successful delivery of the enzyme is shown by red fluorescence, we used Calcein AM, a green dye, to stain the viable cells after the delivery experiment.

Through this platform, we were able to transfect different-sized biomolecules into a variety of cell lines including L929, SiHa, LN-229, and hMSCs. Factors such as the nature of the biomolecule, its size and concentration, as well as laser parameters like laser fluence, exposure duration, and the size and shape of the micro/nanostructure materials, can influence the delivery efficiency and cell viability. Analysis of the delivery efficiency and cell viability was performed using fluorescent microscopy, confocal microscopic imaging, and flow cytometry. Using corresponding bright-field images, the total cell count for each experiment was determined. The delivery efficiency was calculated as the percentage of delivered cells, which are viable,

to the total number of cells (eqn (1)). The cell viability was calculated by taking the ratio of the number of live cells to the total number of cells (eqn (2)). Each experiment was repeated three times under the same experimental conditions, and the results were averaged.

$$\text{Delivery efficiency } (\%) = \left(\frac{N_{dl}}{N_t}\right) \times 100 \quad (1)$$

$$\text{Cell viability } (\%) = \left(\frac{N_{lt}}{N_t}\right) \times 100 \quad (2)$$

where N_{dl} is the total number of delivered and live cells, N_t is the total number of cells, and N_{lt} is the total number of live cells after transfection.

2.8 Methodology for the MTT assay

The cell viability was measured using the MTT colorimetric assay. Cells were seeded in 24-well tissue culture plates at a density of 3×10^4 cells per well in 300 μL of complete culture medium and incubated overnight at 37 °C in a humidified atmosphere with 5% CO_2 to promote cell attachment. After attachment, the cells were treated with the specified experimental conditions, while untreated cells served as controls. The wells containing only the medium were used as blanks.

A stock solution of MTT (3-(4,5-dimethylthiazol-2-yl)-2,5-diphenyltetrazolium bromide) was prepared at a concentration of 5 mg mL^{-1} in sterile phosphate-buffered saline (PBS) and protected from light. After the treatment period, old culture media from each well were replaced with 150 μL of fresh media, and 150 μL of MTT stock solution was added to each well to achieve a final MTT concentration of 2.5 mg mL^{-1}. The plates were then incubated at 37 °C for 4 hours, during which time the viable cells reduced MTT to insoluble purple formazan crystals.

After incubation, the MTT mixed culture medium was carefully removed without disturbing the formazan crystals. The crystals were then solubilized by adding 300 μL of dimethyl sulfoxide (DMSO) to each well and gently shaken for 10 minutes at room temperature to ensure complete dissolving. The absorbance of the resulting solution was measured at 570 nm using a microplate reader.

The cell viability was determined as the percentage of the untreated control using the following equation:

$$\text{Cell viability } (\%) = \frac{(OD_{sample} - OD_{blank})}{(OD_{control} - OD_{blank})} \times 100 \quad (3)$$

where OD is the optical density.

To evaluate cell proliferation over a period, the relative increase in absorbance across various days was analyzed by comparing the MTT signal of each group with that of the untreated control on Day 1. All experiments were conducted in triplicate, and the data are presented as mean ± SD.

$$\text{Cell proliferation } (\%) = \frac{OD_{sample,day\ n} - OD_{blank}}{OD_{control,day\ 1} - OD_{blank}} \times 100 \quad (4)$$

2.9 Device reuse

After each experiment, the micro-patterned rGO device was rinsed with PBS, cleaned with deionized (DI) water, dehydrated under a N_2 flow, and then UV-sterilized for a few hours. After that, the device was ready for the next set of experiments. No performance drop was observed when the device was reused five times (Fig. S2).

3. Results and discussion

3.1 Characterization of synthesized rGO

The GO reduction was observed and monitored using Fourier-transform infrared spectroscopy (FTIR), confocal Raman spectroscopy, and UV-Vis-NIR spectroscopy.

UV-Visible spectroscopy confirmed the formation of reduced graphene oxide, as indicated by a red shift in the absorption peak, due to the restoration of the sp^2 carbon network. Fig. 2(a) shows the UV-Visible spectroscopy results for the synthesized GO and rGO, where GO shows a peak at 235 nm. After GO reduction with a high-power UV source, this peak shifted to 260 nm, possibly due to the restoration of electronic conjugation in the graphene sheets.

During the reduction of GO to rGO, the material undergoes significant structural changes, which can be precisely monitored on the order of micrometers and sub-micrometers using confocal Raman spectroscopy. The successful reduction of GO to rGO was confirmed by the increase in the I_D/I_G ratio, reflecting the formation of new graphitic sites and defects. Since the materials are carbon-based, the prominent bands to be considered here are the D and G bands. Different parameters of these peaks such as position, width, and ratio of intensities of the peaks provide information about the content of sp^3 hybridized carbon atoms, degree of disorder, and size of the crystallite.[66] The resolution between the D and G bands is an indication of the crystallinity of the material. The D band is located at 1330 cm^{-1} to 1360 cm^{-1} It is an indication of defects and disorders present in the structure of the graphitic material. The G band from 1550 cm^{-1} to 1600 cm^{-1} is due to the resonance vibration from the C–C bond stretching. As the GO undergoes reduction, more defects and disorders are introduced in the lattice, which increases the intensity of the D band. The ratio of intensities of the D band and G band (I_D/I_G) can be used to determine the degree of reduction. This ratio I_D/I_G increases as we move from GO to rGO. The confocal Raman spectra for GO and rGO synthesized by reducing GO using high-power UV exposure are shown in Fig. 2(b). Here, we also studied how the time interval of UV exposure for the reduction process affects the degree of reduction of GO. As the UV exposure time interval was varied from 60 to 150 minutes, the degree of reduction increased, indicated by an increase in I_D/I_G ratio. Raman spectroscopy of the corresponding samples indicates these results. Fig. S3 in the SI displays the confocal Raman spectra of rGO nanosheets formed with varying reduction durations, resulting in different I_D/I_G ratios.

Fourier-transform infrared (FTIR) spectroscopy utilizes the interaction of light in the infrared range with matter, thereby aiding in the identification of functional groups present in the sample. FTIR spectroscopy confirmed the reduction of GO to rGO, indicated by the reduction in intensity or disappearance of peaks corresponding to the oxygen-containing functional groups. The FTIR spectrum of graphene oxide is shown in Fig. 2(c). Around 3000 cm^{-1} to 3550 cm^{-1}, there are broad bands of absorption arising from the vibration modes of O–H bonds of alcohols and carboxylic acid groups. These strong, broad bands, due to the presence of hydroxyl groups, clearly account for the hydrophilicity of GO. The stretching vibrational modes can be seen around 1080 cm^{-1} due to C–O epoxide bonds and at 1180 cm^{-1} due to C–OH bonds. At 1720 cm^{-1} the stretching vibrational modes due to the C═O bond in the carboxylic group are seen. Around 1620 cm^{-1}, there are vibrational modes due to C═C phenol ring stretching. The peaks at 1200 cm^{-1} indicate C–O–C stretching and at 1050 cm^{-1} corresponding to C–O groups. The FTIR spectrum of rGO exhibits a significant reduction in the intensity of these peaks, indicating the removal of the majority of oxygen-containing groups from the graphene oxide surface, which ensures a high degree of reduction.

The structure of the rGO nanosheets could be observed using transmission electron microscopy (TEM). The TEM images of the rGO nanosheets synthesized for our experiment are shown in Fig. 2(d). The samples for TEM are prepared by drop-casting a suspension of rGO in ethanol onto TEM grids and then drying them in air. The TEM images show rGO nanosheets of various dimensions with a thickness of few to several layers. The high-magnification TEM image and SAED patterns are shown in Fig. S4 in the SI.

3.2 rGO micro-array device fabrication

Micropatterned rGO structures were fabricated on a glass coverslip using photolithography and UV-assisted photoreduction. The adhesion of UV-reduced graphene oxide (rGO) to the glass (amorphous SiO_2) substrate is mainly driven by non-covalent interfacial interactions rather than direct covalent bonds.[67,68] To confirm the accuracy, uniformity, and quality of the fabricated device, the optical images and scanning electron microscopic (SEM) images were analyzed. Both these methods ensured the successful transfer of the design pattern. The optical (Fig. 3b(i–iii)) and SEM (Fig. 3c(i–iii)) images of the fabricated rGO device comprising rGO islands of 10 μm diameter with an inter-island spacing of 30 μm at different magnifications, are shown in Fig. 3.

To confirm the compositional fidelity and distribution of the micropatterned rGO, complementary elemental analysis was performed using energy-dispersive X-ray spectroscopy (EDS) mapping and confocal Raman mapping. The successful reduction of GO to rGO and the preservation of an sp^2 hybridized carbon network in the patterned area were confirmed by the corresponding Raman spectrum, which exhibited two characteristic bands: D ($\sim$1350 cm^{-1}) and G ($\sim$1580 cm^{-1}). The intensity ratio of the D band and G band (I_D/I_G = 1.1) and the absence of a discernible 2D band indicate the disordered and partially reduced nature of GO, which is typical for rGO. Fig. 4(a) shows the SEM image of the surface topography of the micropatterned device. The circular patches display the rGO islands, with the dark background indicating the glass substrate on which micropatterning is performed. Fig. 4(b) shows the Raman intensity mapping of the characteristic rGO peak at 1580 cm^{-1} visualized over a 2D area similar to the area shown in the SEM image. The bright yellow colour indicates the region with a strong Raman signal intensity, implying a high concentration of rGO, whereas the dark background shows a low or no Raman signal on the bare glass substrate. This confirms the selective deposition of rGO in the desired regions during the fabrication process. Fig. 4(c) shows the Raman cluster image of region mapping. A cluster analysis map is generated during the Raman imaging to differentiate regions based on the spectra. The software statistically groups pixels with identical spectra into a cluster. Here, cluster 1, shown in red, indicates the regions with Raman spectra exhibiting graphene oxide (rGO) features. In contrast, cluster 2, shown in blue, shows the regions that do not exhibit a Raman spectrum with rGO features. Fig. 4(d) shows the spectrum corresponding to cluster 1. The spectrum displays the characteristics of rGO, indicated by the presence of the D band and the G band, and the D/G intensity ratio gives insights into the extent of reduction. Fig. 4(e) shows the Raman spectrum corresponding to cluster 2. The absence of rGO-specific or carbon-specific features in the spectrum confirms the absence of rGO outside the patterned zones. Fig. 4(f) shows the EDS elemental mapping of carbon (C). Supporting the SEM and Raman data, the bright cyan color region, which indicates carbon, exactly matches the patterned region of rGO. Fig. 4(g) and (h) show the EDS maps of oxygen (O) and silicon (Si) across the same region, respectively. However, they are uniformly spread, as both oxygen and silicon are present in the glass substrate, and a small amount of oxygen will also be present in the rGO.

3.3 Immobilized, micropatterned device for intracellular delivery: theoretical understandings

The intricate details of laser-induced temporal and spatial heating processes that facilitate the formation of unstable bubbles were obtained through COMSOL Multiphysics simulation. This model features a 500 nm-thick rGO microstructure on top of a SiO_2 substrate, with water on the other side. Determining the exact absorption energy at each rGO microstructure is a significant challenge. We consider an extinction coefficient of about 1, obtained from ellipsometry measurements.

After photoexcitation with a nanosecond pulsed laser, transient hot carriers are generated through intense carrier-carrier scattering that occurs within a few femtoseconds. Following this, these carriers release energy to the lattice *via* strong carrier-lattice interactions, which occur over a time scale of several hundred femtoseconds to a few picoseconds. These time scales are negligible compared to the pulse duration of the incident laser beam, resulting in instantaneous lattice

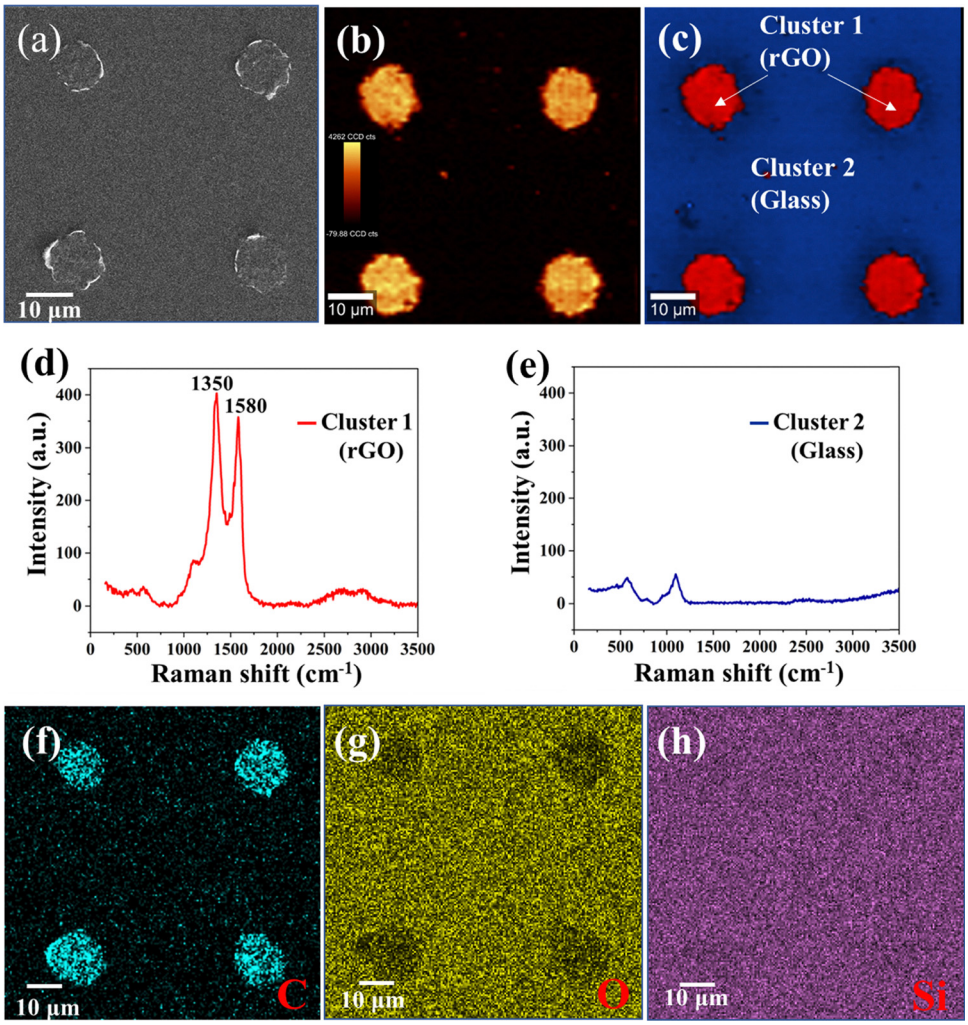

Fig. 4 Comprehensive characterization of the micropatterned rGO on a glass substrate. (a) SEM image of micropatterned rGO on a glass substrate. (b) Two-dimensional Raman intensity mapping corresponding to the characteristic G band. (c) Cluster analysis of Raman mapping differentiating chemically distinct regions, with cluster 1 (red) representing rGO and cluster 2 (blue) corresponding to glass substrate. (d) Raman spectra of cluster 1 showing characteristic D (1350 cm^{-1}) and G (1580 cm^{-1}) bands of rGO. (e) Raman spectra of cluster 2 showing no graphitic features. Energy-dispersive X-ray spectroscopy (EDS) elemental mappings of (f) carbon (C), (g) oxygen (O), and (h) silicon (Si) corresponding to the SEM image.

heating with the arrival of each pulse.[69–71] The hot lattice undergoes cooling through interfacial heat transfer to the surrounding environment, comprising water and the substrate. The simulation utilized a rate equation model to calculate the spatial-temporal temperature distribution.

$$C_e\frac{\partial T_e}{\partial t} = Q(t) - \kappa_e\nabla^2 T_e - \Gamma_{e-ph}[T_e(t) - T_L(t)] \quad (5)$$

$$C_l\frac{\partial T_L}{\partial t} = \Gamma_{e-ph}[T_e(t) - T_L(t)] - \kappa_L\nabla^2 T_L - G_G(T_L - T_G) - G_W(T_L - T_W) \quad (6)$$

$$\rho_W S_W\frac{\partial T_W}{\partial t} = G_W(T_L - T_W) - \kappa_W\nabla^2 T_W - G_{WG}(T_W - T_G) \quad (7)$$

$$\rho_G S_G\frac{\partial T_G}{\partial t} = G_G(T_L - T_G) - \kappa_G\nabla^2 T_G + G_{WG}(T_W - T_G) \quad (8)$$

where $Q(t)$ accounts for heat energy transfer to the carriers due to strong light–matter interactions. It is taken as a Gaussian function, which accounts for a pulse duration of 5 ns. The time integration of this function provides the pulse energy of the incident radiation. Laser-induced heating of the electron and phonon temperatures of rGO are referred to as Te and T_L, respectively. T_W is the water temperature and T_G is the temperature of the glass substrate. The electron and phonon thermal conductivities of rGO are represented by κ_e = 2500 W m^{-1} K^{-1} (ref. 72) and and κ_l = 2000 W m^{-1} K^{-1} (ref. 73) respectively. G_G = 2000 W m^{-1} K^{-1} is the interfacial thermal conductance at the rGO/substrate interface,[74] G_W = 30 MW m^{-2} K^{-1} is the interfacial thermal conductance of the rGO/water interface,[75] and G_{WG} = 330 MW m^{-2} K^{-1} is the interfacial thermal conductance of water/substrate.[76] ρ_G and ρ_W are the mass densities of substrate and water, respectively. S_G and S_W are the specific heats of substrate and water, respectively. κ_G and κ_W are diffusive thermal conductance of

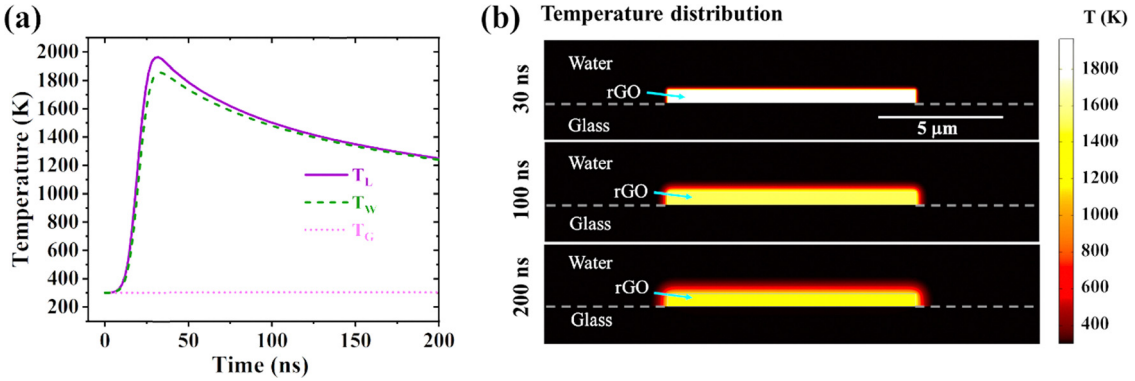

Fig. 5 Simulation results using COMSOL Multiphysics at a fluence of 28 mJ cm^{-2}. (a) Temporal evaluation of rGO, water, and glass substrate temperatures at an arbitrary point at the interface. (b) Special temperature distribution at 30 ns, 100 ns, and 200 ns showing thermal transport from the hot rGO lattice microstructure to the adjacent water.

the substrate and water, respectively. The electron heat capacity $C_e = \alpha T_e^2$, where $\alpha = \frac{18\zeta(3)k_b^3}{\pi\hbar^2 v_f^2}$,[69] assuming rGO to be charge neutral. All the parameters' values are taken from ref. 52 and 77.

At the given fluence of 28 mJ cm^{-2}, the temporal and spatial temperature distributions are shown in Fig. 5(a) and (b), respectively. It is essential to note that both the carriers and the phonons experience heating throughout each pulse. Nonetheless, the rate at which thermal energy dissipates into the surrounding environment, including water and the substrate, is relatively low, resulting in prolonged hot phonons—the bottleneck effect. The lattice temperature (T_L) decreases very slowly, as shown in Fig. 5(a), due to this bottleneck effect. At the interface, the substrate temperature T_G shows negligible change throughout 200 ns, indicating very slow heat transfer into it. However, the water temperature (T_W) rises at the interface following T_L. The difference in T_L and T_W was maintained for an extended duration of 100 ns. In the case of the gold/water interface, when the interface temperature rises above 550 K, bubble generation starts to occur.[78] Similarly, this study shows an elevated T_W far above 550 K, leading to unstable bubble formation. The simulation does not account for the material's phase transitions and does not include convective flow. In practice, both can be present. The generated bubbles are unstable—they grow, coalesce, and collapse, resulting in jet flow and turbulence near the cell membrane, which creates temporary openings in the membrane that allow foreign biomolecules to enter the cytoplasm.

3.4 Intracellular delivery of the PI dye

To optimize the laser parameters with our model dye (PI dye), we set the motorized scanning stage speed at 15 mm s^{-1} and gradually increased the laser fluence value while maintaining a fixed laser wavelength of 1064 nm. We could see some PI dye delivery (30%) at a lower fluence starting from 20 mJ cm^{-2}. However, the maximum delivery efficiency (97%) and cell viability (98.5%) were achieved at 28 mJ cm^{-2} in LN-229 cells. Fig. 6(a) shows the variation in delivery efficiency and cell viability for varied pulse laser fluence in LN-229 cells. The delivery efficiency (70%) and cell viability (70%) were reduced upon further increase in laser fluence (36 mJ cm^{-2}), possibly due to the cell membrane damage caused by excessive heating and irreversible membrane sealing.[10,37] The SI (Fig. S5) shows the bright-field and PI dye delivery images of LN-229 cells for a laser fluence varying from 20 mJ cm^{-2} to 36 mJ cm^{-2} at 1064 nm at a scanning speed of 15 mm s^{-1}. We also studied the effect of varying scanning speed on cell viability and PI delivery efficiency, and the results are presented in the SI (Fig. S6 and S7). Moreover, we performed a control experiment (Fig. S8), where a laser was exposed to LN-229 cells without a micro-patterned rGO device, confirming the absence of PI delivery into the cells without an rGO device. Further, we conducted experiments without laser exposure on LN-229 cells incubated with the PI dye, using a micro-patterned rGO device aligned on top of the cells. The results confirmed that there is no PI delivery in the absence of the laser exposure. To validate our assumption regarding interisland spacing and the number of contact points, which we considered during device design, we conducted intracellular delivery experiments using devices with different interisland spacings, while keeping all other experimental parameters constant. The results are shown in Fig. S9 of the SI, aligning with our hypotheses and demonstrating a uniform delivery for an inter-island spacing of 30 μm.

Results were analyzed both manually and using the ImageJ software. For intracellular delivery experiments with the PI dye, the best results were achieved using a 10 μg mL^{-1} concentration. Above this concentration, the viability of the cells started to decrease. Fig. 6(b) presents the quantitative analysis of delivery efficiency and cell viability for varying PI dye concentrations in LN-229 cells at a laser fluence of 28 mJ cm^{-2}. The best outcomes were observed at 15 mm s^{-1} scanning speed with a PI concentration of 10 μg mL^{-1} for LN-229 cells with a delivery efficiency of 97% and a cell viability of approximately 98.5%, while a higher scanning speed shows a lower delivery efficiency due to less exposure time, and a lower density of pore formation or faster resealing time, leading to reduced dye

diffusion. Again, a lower scanning speed results in lower delivery efficiency and lower cell viability, which may be due to a higher exposure time leading to increased cell death, thereby reducing the number of live cells delivered. Thus, the

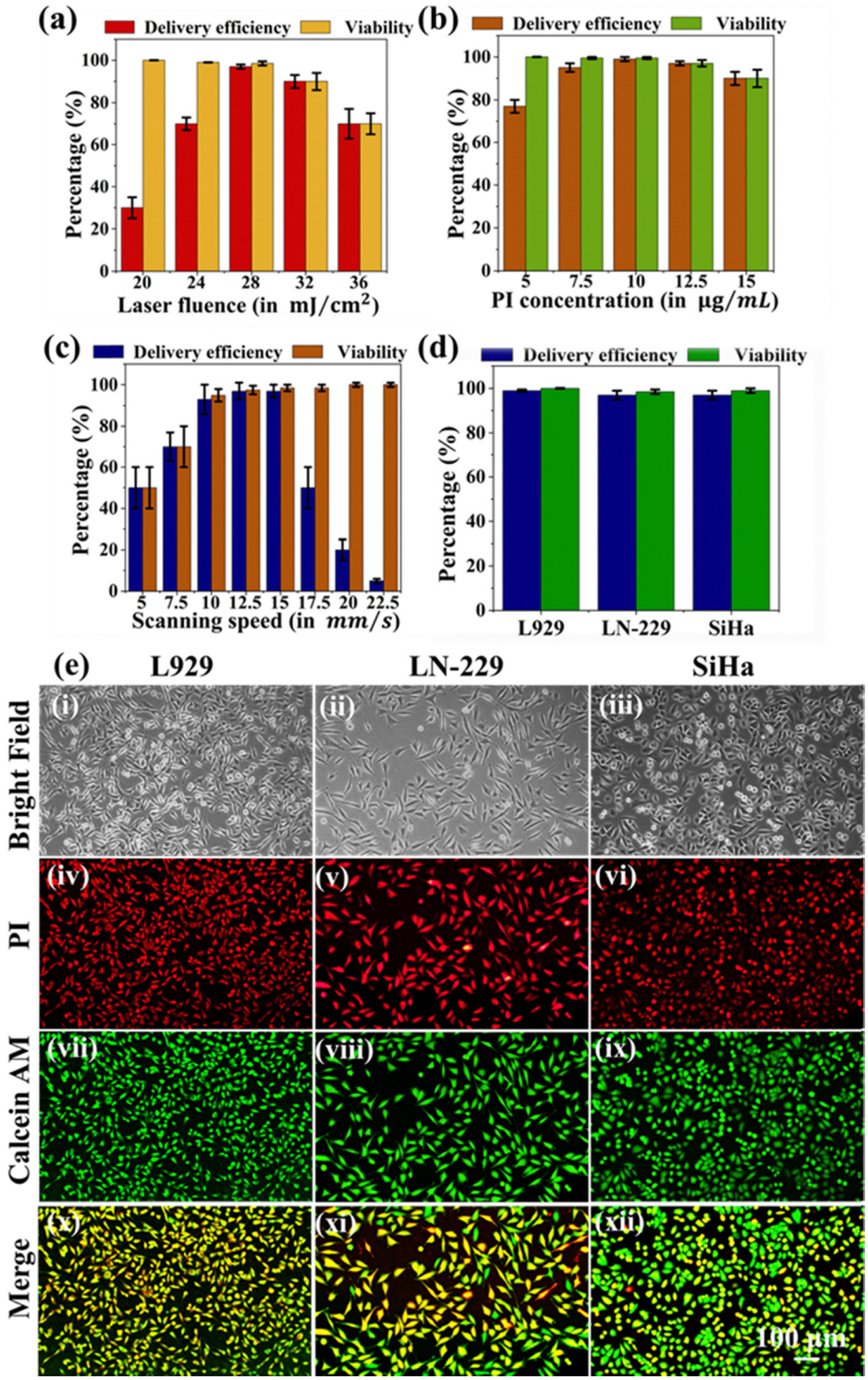

Fig. 6 Intracellular delivery of the PI dye using the micro-patterned rGO device. (a) Variation in the PI dye delivery efficiency and cell viability for varied laser fluence at a constant scanning speed of 15 mm s^{-1}, performed in LN-229 cells. (b) Effect of the PI dye concentration on the delivery efficiency and cell viability. (c) The effect of the variation in laser scanning speed on the PI dye delivery efficiency and cell viability at a constant laser fluence of 28 mJ cm^{-2}. (d) Delivery efficiency and cell viability in various cell lines with a laser fluence of 28 mJ cm^{-2} and a scanning speed of 15 mm s^{-1}. (e) Bright-field (i–iii) and fluorescence images (red: delivered (iv–vi); green: live cells (vii–ix); and yellow to greenish yellow: delivered and live cells (x–xii)) of the intracellular delivery of PI dye in L929, LN-229, and SiHa cells. The images were taken 30 minutes post-PI delivery experiments.

optimized scanning speed is necessary to achieve the best delivery efficiency and cell viability. Fig. 6(c) shows the quantification of these data. Fig. 6(d) shows the quantification of results for PI dye delivery experiments in different cell lines using 28 mJ cm^{-2} laser fluence at a wavelength of 1064 nm with a scanning speed of 15 mm s^{-1} and a PI dye concentration of 10 μg mL^{-1}. The best results were achieved using L929 cells, which demonstrated 99% delivery efficiency and nearly 100% cell viability, compared to the other cell lines. Fig. 6(e) shows the corresponding bright-field and fluorescence microscopic images for PI dye delivery and cell viability for L929, SiHa, and LN229 cells. The red fluorescence images indicate PI dye delivery, while green fluorescence images indicate cell viability after PI dye delivery, and green to yellowish green cells confirm the cell viability post-PI dye delivery.

3.5 Transfection of siRNA

We found that the best siRNA transfection efficiency (98%) can be achieved at a laser scanning speed of 10 mm s^{-1} for L929 cells. Moreover, we observed that a lower scanning speed (10 mm s^{-1}) was required for most successful siRNA transfection compared to the PI dye delivery (15 mm s^{-1}). This can be due to the larger size of siRNA, which may require a longer exposure time. Since siRNA expression is visualized as green fluorescence, after the photoporation experiment, we used Calcein red-orange AM to stain the live cells.

Fig. 7 summarizes the results for siRNA transfection across different cell lines. Fig. 7(a) shows the quantitative analysis for transfection efficiency and cell viability across varied siRNA concentrations in LN-229 cells, and the best-optimized siRNA concentration was found to be 2 μM to achieve maximum transfection efficiency (97%) and cell viability (99%). Fig. 7(b) demonstrates the efficacy of siRNA transfection and cell viability achieved in different cell lines. The transfection efficiency and cell viability were 98% and 99%, respectively, for L929 cells. For the SiHa and LN-229 cell lines, the transfection efficiencies were 96.5% and 97%, respectively, and the corresponding cell viabilities were 98.5% and 99%. Fig. 7(c) shows the flow cytometry histogram quantifying the percentage of transfected and live L929 cells following siRNA transfection. Fig. 7(d) shows the fluorescence microscopic images of siRNA transfection, where green fluorescence confirms siRNA transfection of L929, SiHa, and LN229 cells, red fluorescence corresponds to viable cells after photoporation, and merged images with green to yellowish-green fluorescence confirm viable cells. Moreover, to confirm siRNA transfection, we conducted confocal microscopy with 3 μm step size (Z scanning). Fig. 7(e) shows the confocal microscopic images of L929 cells, which confirmed the siRNA transfection (green), cell viability (red), cell nucleus (blue) and merged images of green and red, which produced green to yellowish green fluorescence confirming live cells after siRNA transfection.

Moreover, we conducted control experiments in which two sets of LN-229 cells were subjected to laser exposure. One set was without a micro-patterned rGO device, and another set had the device aligned on top of the cells. In both cases, the laser parameters were kept at the optimized values (1064 nm, 28 mJ cm^{-2}, 10 mm s^{-1}, and 2 μM siRNA) for successful siRNA transfection. After the experiment, we found that LN-229 cells exposed to laser in the presence of a micro-patterned rGO device successfully achieved siRNA transfection. In contrast, the control or second set of LN-229 cells did not express siRNA, indicating the role of the micro-patterned rGO device in successful siRNA transfection. Fluorescence microscopic images corresponding to this control experiment are shown in Fig. S10 of the SI.

3.6 Transfection of enhanced green fluorescence protein (EGFP)

With an optimized scanning speed of 7 mm s^{-1} and a fluence of 28 mJ cm^{-2}, we were able to see successful EGFP transfection in LN-229 cells (Fig. 8(a)), with a transfection efficiency of 98.5% and a cell viability of 99%. Fig. 8(b) shows the EGFP transfection efficiency and cell viability across different cells, and the best transfection efficiency of 98.5% and cell viability of 99% were achieved using LN-229 and SiHa cells. For L929 cells, the EGFP transfection efficiency and cell viability were 97% and 98%. Fig. 8(c) shows the flow cytometry histogram quantifying the percentage of transfected and live SiHa cells following EGFP transfection. Fig. 8(d) displays the fluorescence microscopic images of EGFP expression, where successful EGFP transfection was indicated with green fluorescence in L929, SiHa, and LN-229 cells. The corresponding red signal from Calcein, which is red-orange, indicated cell viability after photoporation experiments. Merged images with a green to yellowish green colour confirmed the viability of successfully transfected cells. Moreover, to confirm EGFP expression (Fig. 8(e)), we performed confocal microscopy. The image with a green colour confirmed successful EGFP expression after 24 hours of EGFP delivery. The red colour confirmed cell viability. The blue image shows the live cell nucleus with Hoechst 33342 staining, and the merged image, from green to yellowish green, confirms cell viability after EGFP transfection.

Control experiments were conducted, where L929 cells incubated with EGFP plasmids were exposed to laser in the presence and absence of the micro-patterned rGO device. Fig. S11 of the SI confirmed that there is no EGFP expression with laser exposure, without a micro-patterned rGO device. Moreover, the experiment also confirmed that there is no EGFP expression in the absence of laser exposure, in the presence of micro-patterned rGO device. These results demonstrate the importance of combining a micro-patterned rGO device with a pulse laser in achieving successful EGFP expression, characterized by high transfection efficiency and cell viability.

3.7 β-Galactosidase enzyme transfection

Successful β-galactosidase enzyme transfection was achieved across different cell lines using an optimized enzyme concentration of 22.5 U mL^{-1} at a scanning speed of 5 mm s^{-1}. Fig. 9(a) shows β-galactosidase enzyme transfection into L929 cells with different enzyme concentrations. The best results were achieved with a concentration of 22.5 U mL^{-1}. Fig. 9(b)

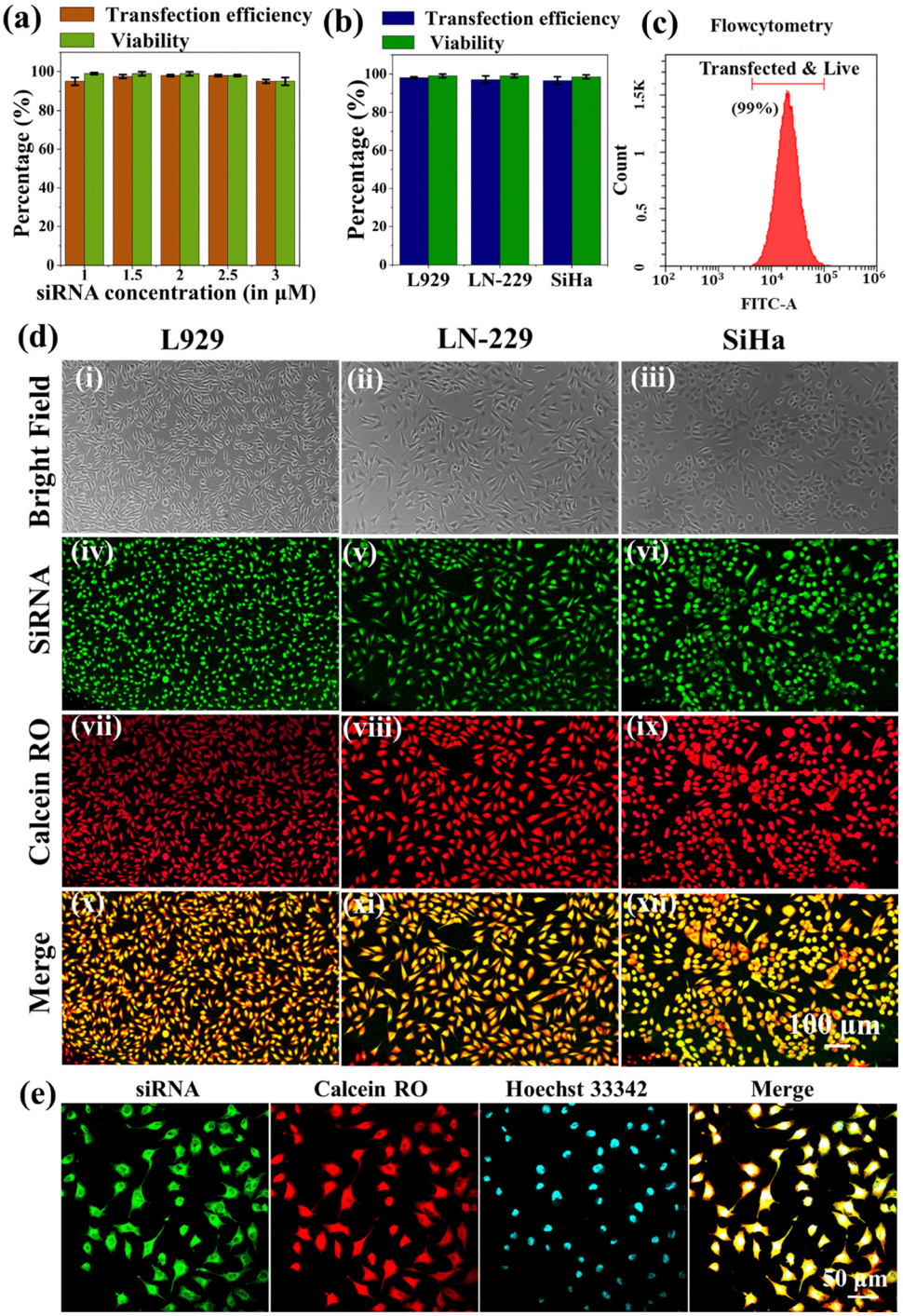

Fig. 7 The siRNA transfection using the micro-patterned rGO device. (a) Efficacy of siRNA transfection and cell viability in L929 cells across varied siRNA concentrations. (b) Efficiency of siRNA transfection and cell viability in L929, SiHa, and LN-229 cells using an siRNA concentration of 2 μM. (c) Flow cytometry histogram quantifying the percentage of transfected and live L929 cells after the siRNA transfection. (d) Bright-field (i)–(iii) and fluorescence (iv)–(vi) (green) images of siRNA transfection in L929, SiHa, and LN-229 cells, corresponding cell viability (vii)–(ix) (red) and merged images of green to yellowish green (x)–(xii) showing live cells after siRNA transfection. (e) Confocal microscopy images of L929 cells after successful siRNA transfection (green), cell viability (red), cell nucleus (blue) and merged image of green to yellowish green confirmed live cells. The images were taken 24 hours after siRNA transfection.

presents the enzyme transfection efficiency and cell viability in different cell lines such as L929, SiHa, and LN-229 with an optimized enzyme concentration of 22.5 U mL^{-1} and a scanning speed of 5 mm s^{-1}. The transfection efficiencies and cell viabilities in L929 and SiHa cells were 98% and 96.5%, and 99% and 99%, respectively. For LN-229 cells, the

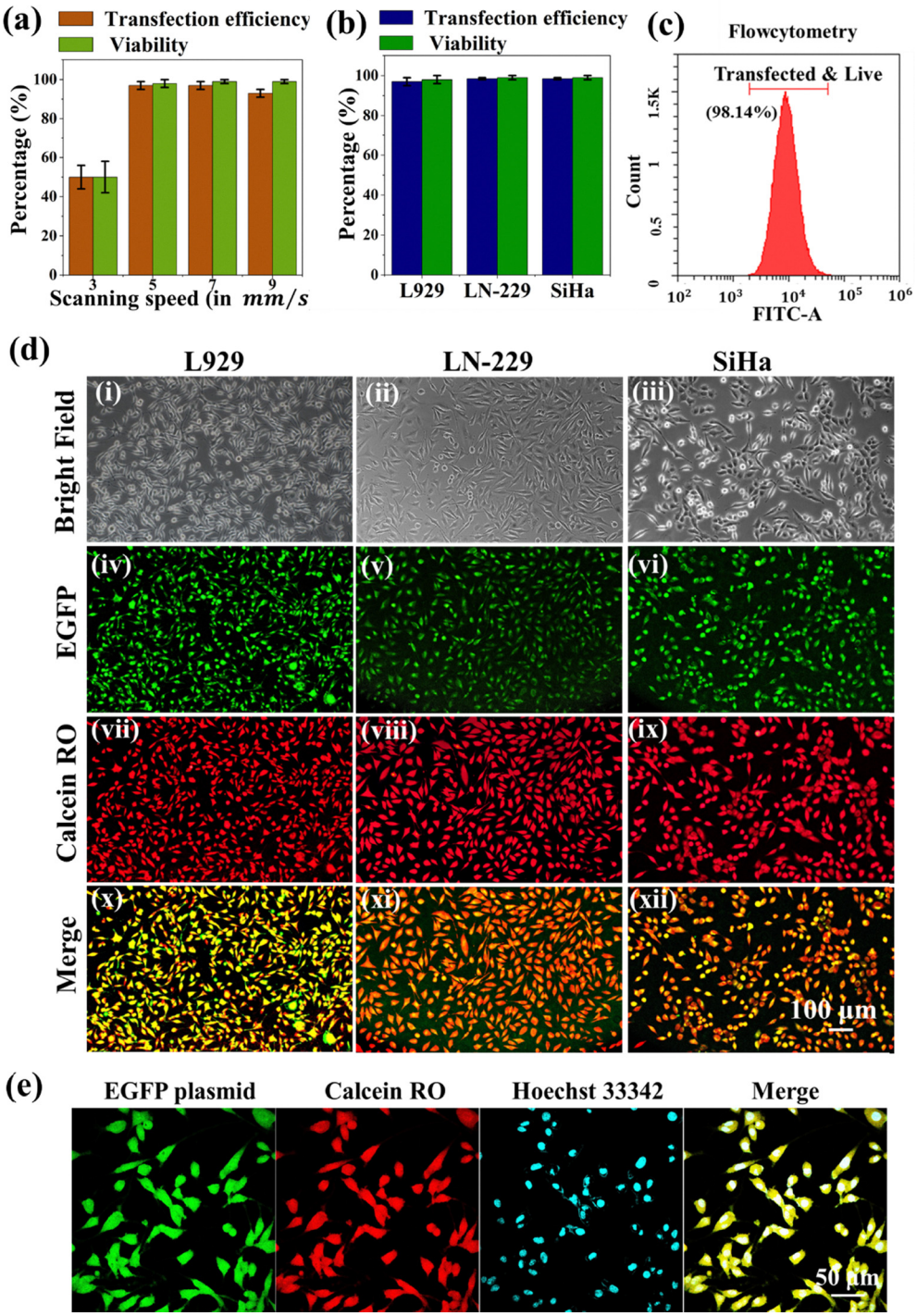

Fig. 8 Transfection of the plasmid for EGFP expression using the micro-patterned rGO device. Graphical plot showing (a) transfection efficiency and cell viability in L929 cells at different laser scanning speeds and (b) plasmid transfection efficiency and cell viability in L929, SiHa, and LN-229 cells using an EGFP concentration of 125 μg mL^{-1} at a scanning speed of 7 mm s^{-1}. (c) Flow cytometry histogram quantifying the percentage of transfected and live SiHa cells after the EGFP plasmid transfection. (d) Bright-field (i)–(iii) and fluorescence (iv)–(vi) (green) images of EGFP plasmid transfection in L929, SiHa, and LN-229 cells, corresponding to cell viability (vii)–(ix) (red), and merged images of green to yellowish green (x)–(xii) confirmed live cells after EGFP plasmid transfection. (e) Confocal microscopy images (SiHa cells) of cells after successful transfection of the plasmid for EGFP expression (green), cell viability (red), cell nucleus staining (blue) using Hoechst 33342 and merged image of green to yellowish green confirmed the cell viability after transfection. The images were taken 24 hours post-plasmid transfection experiments.

transfection efficiency and cell viability were 95% and 98%, respectively. Fig. 9(c) shows the fluorescence microscopic images of enzyme transfection (red) in L929, SiHa, and LN-229 cells, and the corresponding Calcein AM (green) staining confirmed the viability of cells post-transfection. The merged image, with green to yellowish green, confirmed that

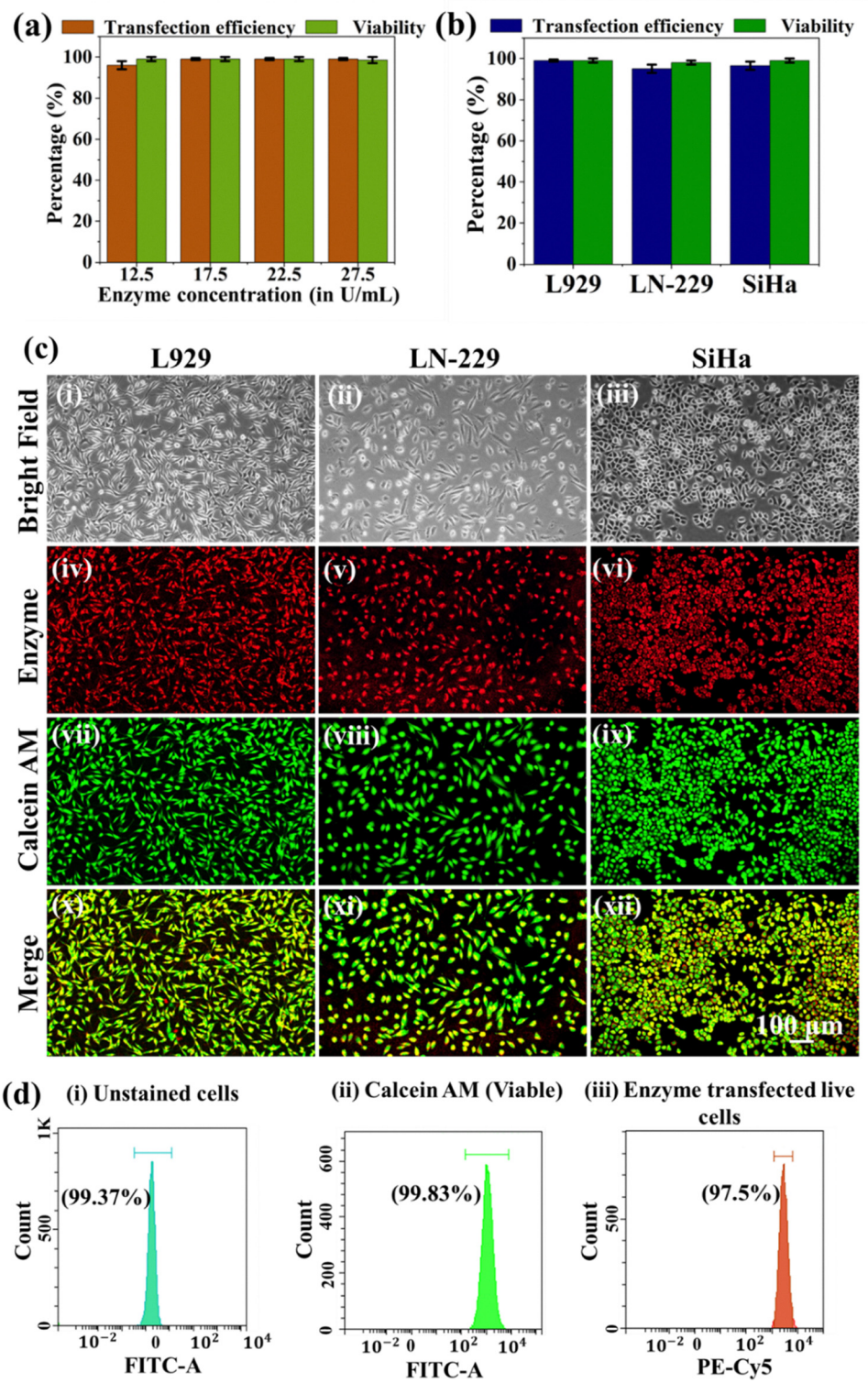

Fig. 9 Intracellular enzyme delivery using the micro-patterned rGO device. Graphical plot showing (a) transfection efficiency and cell viability in L929 cells with different concentrations of the enzyme and (b) transfection efficiency and cell viability of L929, SiHa, and LN-229 cells using an enzyme concentration of 25 U mL^{-1} at a scanning speed of 5 mm s^{-1}. (c) Fluorescence microscopy images of cells after successful enzyme delivery (red (iv–vi)) and the corresponding cell viability (green (vii–ix)), and merged images (x–xii) of green to yellowish green confirmed the cell viability. (d) Flow cytometry results for enzyme transfection in L929 cells: (i) total count of unstained cells, (ii) viable cells and (iii) the count of both successfully transfected cells and viable cells. The images were taken 24 hours post-enzyme transfection experiments.

the transfected cells are viable. The flow cytometry (BD FACS CANTO II, USA) analysis further confirmed the results. Fig. 9(d) shows the results of flow cytometry analysis performed after transfecting the β-galactosidase enzyme into L929 cells: (i) unstained total cell count, (ii) viable cells (Calcein AM-positive) after enzyme transfection, and (iii) enzyme-transfected viable cells (both Calcein AM- and β-galactosidase enzyme-Cy5-positive). Three independent experiments were conducted, and the results were consistent with those from the image analysis.

The control experiments were conducted (Fig. S12), where we exposed L929 cells to laser in the presence and absence of a micro-patterned rGO device. The results confirmed that there was no enzyme transfection with laser exposure and without a micro-patterned rGO device. Fig. S13 shows the fluorescence images corresponding to enzyme transfection for varied enzyme concentrations of 17.5 U mL^{-1}, 22.5 U mL^{-1}, and 27.5 U mL^{-1}. For a lower concentration of 17.5 U mL^{-1}, the red fluorescence signal is weak, whereas for a higher concentration of 27.5 U mL^{-1}, the background increases and there is a slight decrease in cell viability.

3.8 PI dye delivery and enzyme transfection in hMSCs

Following the successful delivery of different-sized biomolecules to L929, SiHa, and LN-229 cell lines, the micro-patterned rGO device was utilized for transfecting human mesenchymal stem cells (hMSCs). We chose to deliver the smallest biomolecule, PI dye (668 Da), and the largest biomolecule, β-galactosidase enzyme (465 kDa), into human mesenchymal stem cells (hMSCs). The same experimental parameters were used for the corresponding molecule, *i.e.*, 1064 nm, 28 mJ cm^{-2}, and 15 mm s^{-1} for PI dye delivery and 1064 nm, 28 mJ cm^{-2}, and 5 mm s^{-1} for enzyme delivery. We successfully achieved the delivery of PI dye and β-galactosidase enzyme into hMSCs. The PI dye delivery efficiency and cell viability for hMSCs were 96% and 99%, respectively. For the enzyme, the transfection efficiency and cell viability were 94% and 99%, respectively.

Fig. 10(a) and (b), respectively, show bright-field and fluorescence microscopic images of PI dye and enzyme transfection in hMSCs. The red fluorescence corresponds to the delivery of the PI dye and enzyme transfection. The Calcein AM staining (green) indicates the live cell images after PI dye delivery and enzyme transfection. The merged images with green to yellowish green fluorescence verify the viability of hMSCs after successful PI dye delivery and enzyme transfection. Fig. 10(c) and (d) show the histograms obtained in the flow cytometry analysis performed after the delivery of PI dye and transfection of β-galactosidase enzyme in hMSCs. Three independent experiments were considered for each case. Fig. 10(c) shows flow cytometry histograms for PI dye delivery experiments, with Fig. 10(c)(i) showing the unstained total cell count, Fig. 10(c)(ii) showing viable cells (Calcein AM positive) after the delivery experiment, and Fig. 10(c)(iii) showing PI dye-delivered viable cells (both Calcein AM and PI dye positive). Fig. 10(d) shows flow cytometry histograms for Cy5-labeled β-galactosidase enzyme transfection experiments, with Fig. 10(d)(i) showing the unstained total cell count, Fig. 10(d)(ii) showing viable cells (Calcein AM positive) after the transfection experiment, and Fig. 10(d)(iii) showing enzyme-transfected viable cells (both Calcein AM and β-galactosidase enzyme-Cy5 positive). The results were found to be consistent with the image analysis results. Fig. 10(e) shows a quantitative analysis of the delivery efficiency and cell viability for PI dye delivery and enzyme transfection in hMSCs.

3.9 Biocompatibility evaluation of the micro-patterned rGO photoporation platform

For the cytotoxicity test, a control experiment was conducted, where neither laser was exposed to a monolayer of cells, nor were cells exposed to the micro-patterned rGO device. A monolayer of cells, which was exposed to laser (28 mJ cm^{-2}, 1064 nm, 5 mm s^{-1}) without the rGO device, was considered as sample 1, and cells exposed to laser (28 mJ cm^{-2}, 1064 nm, 5 mm s^{-1}) with the rGO device were considered as sample 2. After the laser exposure, cells were incubated for 30 minutes, and live (Calcein AM) and dead (PI) cell staining was performed. From the fluorescence microscopic images, it was concluded that cell viability was not affected by laser exposure in the presence or absence of the rGO device. This demonstrates that neither laser exposure nor the rGO device generates cytotoxicity during intracellular delivery experiments. Fluorescence images corresponding to this experiment are given in Fig. S14 of the SI.

Moreover, the cytotoxicity effect of the micro-patterned rGO device-based photoporation platform was assessed using the 3-(4,5-dimethylthiazol-2-yl)-2,5-diphenyltetrazolium bromide (MTT) assay (analytical grade, TCI, Japan). The 3-day MTT experiments were conducted for both the control and the three samples, and all experiments were conducted in triplicate; the average of the results was then taken. The control contained unexposed cells that were neither exposed to laser scanning nor to a micro-patterned rGO device. The first sample consisted of cells exposed to laser scanning without a micro-patterned rGO device. The second sample consisted of cells exposed to the micro-patterned rGO device but not to the laser. The third sample consisted of cells exposed to laser scanning with the micro-patterned rGO device. The laser parameters used for preparing the samples were a laser fluence of 28 mJ cm^{-2} at a wavelength of 1064 nm and a minimum scanning speed of 5 mm s^{-1}, which correspond to the largest biomolecule (enzyme). This setup allows the study of the effect of maximum laser exposure on cells in our work. To analyze the viability and proliferation of exposed samples, MTT assays were performed over 3 days, and the optical density (OD) was measured at 570 nm. The absorbance values were then converted into percentages of cell viability and cell proliferation. The detailed procedure and calculation methods for the MTT assay are described in the methodology section.

As expected, the control showed the highest viability and proliferation in all cell lines. Moreover, our experimental samples demonstrated good viability and proliferation, although slightly less than the control, as shown for L929 cells

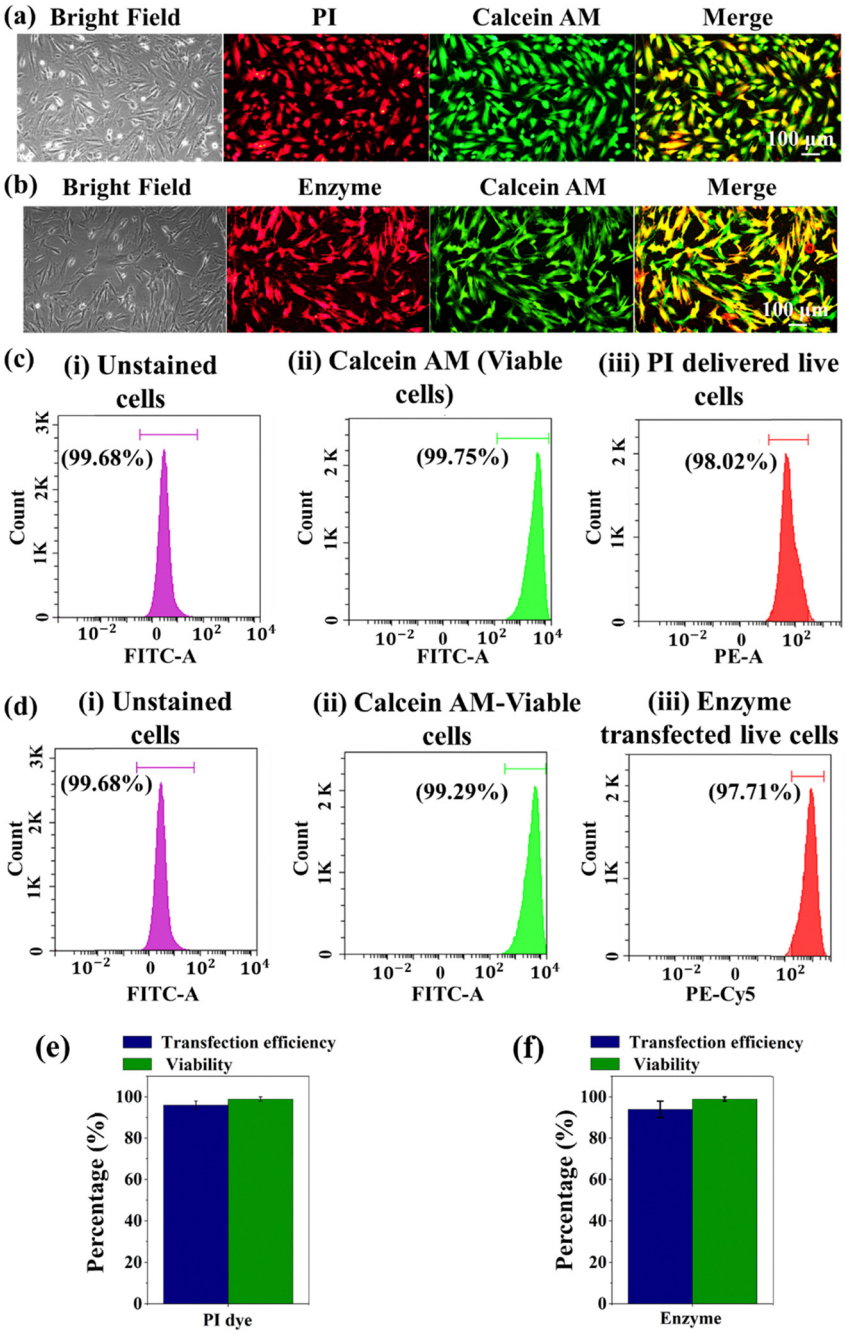

Fig. 10 Intracellular delivery of the PI dye and enzyme in hMSCs using the micro-patterned rGO device. (a) Bright-field and fluorescence microscopy images of cells following successful PI dye delivery (red) and the corresponding cell viability (green), and the merged image of green to yellowish green validated the cell viability post-PI dye delivery. The images were taken 30 minutes post-PI delivery experiments. (b) Bright-field and fluorescence microscopy images of the successful β-galactosidase enzyme transfection (red) and the corresponding cell viability (green), and the merged image of green to yellowish green validated viability of cells post-enzyme transfection. The images were taken 24 hours post-enzyme transfection experiments. (c) Flow cytometry histograms for PI delivery: (i) unstained total cell count, (ii) viable cells, and (iii) delivered and live. (d) Flow cytometry histograms for enzyme transfection: (i) unstained total cell count, (ii) viable cell count, and (iii) transfected and live cell count. (e) Quantification of the delivery efficiency and cell viability for the PI dye delivery and β-galactosidase enzyme transfection.

in Fig. 11. When the samples were compared, although the sample exposed to both the laser and the micro-patterned rGO device showed slightly lower cell viability on the first day, the proliferation rate was comparable to that of the control. The initial reduction in viability can be attributed to the added stress from the device and laser fluence, but the change was not very significant. The plots showing raw absorbance values (for all experimental conditions for each day) and the corresponding calculated cell proliferation for SiHa cells (Fig. S15 and S16), LN229 cells (Fig. S17 and S18) and L929

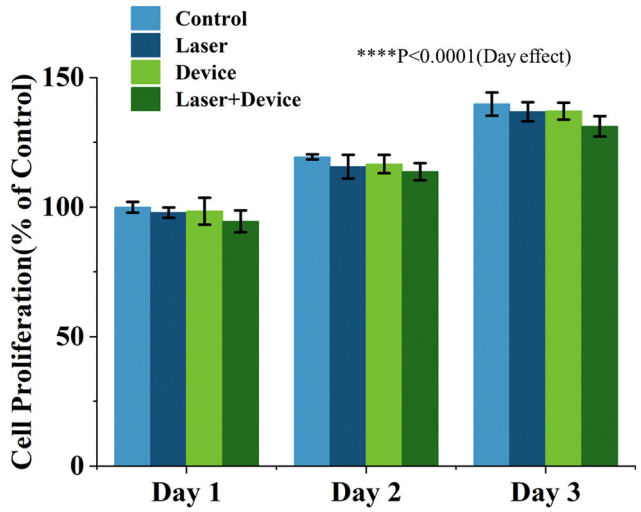

Fig. 11 Quantification of the 3-day MTT assay for the L929 cells that were neither subjected to laser exposure nor exposed to the rGO device (Control), cells that were subjected to laser exposure without the micro-patterned rGO device (Laser), cells exposed to rGO device with no laser exposure (Device), and cells that were subjected to laser exposure with the micro-patterned rGO device aligned on top of cells (Device + Laser). Data represent mean ± SD (n = 3). MTT assay results (mean ± SD and n = 3) show a progressive increase in metabolic activity from day 1 to day 3 across all groups (two-way RM ANOVA: day effect, ****$p < 0.0001$), confirming time-dependent cell proliferation. Although the overall treatment effect was statistically significant (p = 0.0381), Tukey's multiple comparisons revealed no significant differences among groups within any day ($p > 0.2$ for all).

cells (Fig. S19 and S20) are given in the SI. The calculated cell viability was 95.4% for SiHa cells, 96% for LN229 cells, and 94.5% for L929 cells.

In summary, both live-dead cell staining and MTT assay results indicated that neither the laser exposure nor the micro-patterned rGO device introduced any cytotoxicity to the cells. Tables S1 and S2 in the SI show the two-way RM ANOVA results and Tukey's multiple comparisons, respectively.

To obtain a more precise quantification of the cell proliferation profile, we tracked cell counts for 7 days post-photoporation. Fig. S21 in the SI shows the graphical plot for this study. Comparison with an untreated control did not show a significant reduction in cell survival or proliferation, indicating the biocompatibility of our platform and its suitability for repeated and long-term photoporation experiments.

4. Conclusion

This study successfully developed and demonstrated an immobilized, micro-patterned rGO device-based photoporation platform for the fast and efficient intracellular delivery of cargos across various cell types, including human mesenchymal stem cells (hMSCs). By combining the advantages of the photothermal properties of rGO with a spatially defined microarray design and the precision of near-infrared nanosecond pulse laser-based scanning systems, this platform could achieve controlled cell plasma membrane permeabilization with minimal cell toxicity and exceptional throughput. As evidenced, our platform can deliver a broad spectrum of biomolecules including PI dye, siRNA, a plasmid for EGFP expression, and enzymes into various cell lines including clinically relevant human mesenchymal stem cells (hMSCs).

The micropatterning of rGO islands facilitates uniform energy distribution and localized heating, thereby eliminating the disadvantages of free nanoparticle-mediated photoporation, including nanoparticle aggregation, non-uniform energy distribution, nonspecific heating, and cellular uptake. The immobilization of rGO enhanced the platform's biocompatibility, allowing for repeatable localized photoporation. Our device demonstrates significant potential as a versatile and scalable tool for intracellular delivery, applicable in areas ranging from cell-based therapies and gene therapy to drug screening and regenerative medicine. The ability of this platform to transfect a million cells in a few seconds with high viability makes it a potential candidate for both *in vitro* and translational medicine applications.

However, further study is required to expand this platform to broader *in vivo* applications. Future studies will focus on integrating this work into *in vivo* and 3D tissue culture models, as well as incorporating an automated laser scanning system with real-time feedback loops for dynamic control of delivery parameters.

Conflicts of interest

The authors declare that they have no competing financial interests or personal relationships that could be perceived to influence the work reported in this paper.

Data availability

Data will be made available on request.

Supplementary information (SI) is available. See DOI: https://doi.org/10.1039/d5ma01317h.

Acknowledgements

This work was supported by the Science and Engineering Research Board (SERB), Grant CRG/2022/003167, Government of India, awarded to Dr Tuhin Subhra Santra. The work is also supported by the INSPIRE Faculty Fellowship Grant, DST/INSPIRE/04/2021/001032, Department of Science and Technology (DST), Government of India, awarded to Dr Srabani Kar.

References

1 D. Morshedi Rad, M. Alsadat Rad, S. Razavi Bazaz, N. Kashaninejad, D. Jin and M. Ebrahimi Warkiani, A Comprehensive Review on Intracellular Delivery, *Adv. Mater.*, 2021, **33**(13), e2005363, DOI: 10.1002/adma.202005363.

2 M. P. Stewart, R. Langer and K. F. Jensen, Intracellular Delivery by Membrane Disruption: Mechanisms, Strategies,

and Concepts, *Chem. Rev.*, 2018, 7409–7531, DOI: 10.1021/acs.chemrev.7b00678.

3 N. Nayerossadat, T. Maedeh and P. Ali, Viral and Nonviral Delivery Systems for Gene Delivery, *Adv Biomed Res*, 2012, **1**(1), 27, DOI: 10.4103/2277-9175.98152.

4 S. Ghosh, A. M. Brown, C. Jenkins and K. Campbell, Viral Vector Systems for Gene Therapy: A Comprehensive Literature Review of Progress and Biosafety Challenges, *Appl. Biosaf.*, 2020, 7–18, DOI: 10.1177/1535676019899502.

5 T. K. Kim and J. H. Eberwine, Mammalian Cell Transfection: The Present and the Future, *Anal. Bioanal. Chem.*, 2010, **397**(8), 3173–3178, DOI: 10.1007/s00216-010-3821-6.

6 Z. X. Chong, S. K. Yeap and W. Y. Ho, Transfection Types, Methods and Strategies: A Technical Review, *PeerJ*, 2021, **9**, e11165, DOI: 10.7717/peerj.11165.

7 K. Kaladharan, A. Kumar, P. Gupta, K. Illath, T. S. Santra and F. G. Tseng, Microfluidic Based Physical Approaches towards Single-cell Intracellular Delivery and Analysis, *Micromachines*, 2021, **12**(6), 631, DOI: 10.3390/mi12060631.

8 J. M. Meacham, K. Durvasula, F. L. Degertekin and A. G. Fedorov, Physical Methods for Intracellular Delivery: Practical Aspects from Laboratory Use to Industrial-Scale Processing, *SLAS Technol.*, 2014, **19**(1), 1–18, DOI: 10.1177/2211068213494388.

9 M. P. Stewart, A. Sharei, X. Ding, G. Sahay, R. Langer and K. F. Jensen, In Vitro and Ex Vivo Strategies for Intracellular Delivery, *Nature*, 2016, 183–192, DOI: 10.1038/nature19764.

10 A. S. Shinde, P. Shinde, M. Nagai, S. Kar and T. S. Santra, Infrared Light Activated Highly Efficient Cell Therapy Using Flower-Shaped Microstructure Device, *Adv. Ther.*, 2024, **7**(11), 2400046, DOI: 10.1002/adtp.202400046.

11 K. Illath, S. Kar, A. Shinde, R. Ojha, D. R. Iyer, N. R. Mahapatra, M. Nagai and T. S. Santra, Microfluidic Device-Fabricated Spiky Nano-Burflower Shape Gold Nanomaterials Facilitate Large Biomolecule Delivery into Cells Using Infrared Light Pulses, *Lab Chip*, 2023, **23**(22), 4783–4803, DOI: 10.1039/d3lc00341h.

12 S. Bao, B. D. Thrall and D. L. Miller, Transfection of a Reporter Plasmid into Cultured Cells by Sonoporation in Vitro, *Ultrasound Med. Biol.*, 1997, **23**(6), 953–959, DOI: 10.1016/S0301-5629(97)00025-2.

13 S. Kar, M. Loganathan, K. Dey, P. Shinde, H.-Y. Chang, M. Nagai and T. S. Santra, Single-Cell Electroporation: Current Trends, Applications and Future Prospects, *J. Micromech. Microeng.*, 2018, **28**(12), 123002, DOI: 10.1088/1361-6439/aae5ae.

14 T. S. Santra, C. W. Chen, H. Y. Chang and F. G. Tseng, Dielectric Passivation Layer as a Substratum on Localized Single-Cell Electroporation, *RSC Adv.*, 2016, **6**(13), 10979–10986, DOI: 10.1039/c5ra18258a.

15 A. Kumar, B. K. Nahak, P. Gupta, T. S. Santra and F. G. Tseng, Laser-Induced Intracellular Delivery: Exploiting Gold-Coated Spiky Polymeric Nanoparticles and Gold Nanorods under Near-Infrared Pulses for Single-Cell Nano-Photon-Poration, *Micromachines*, 2024, **15**, 168, DOI: 10.3390/mi15020168.

16 J. Tu and A. C. H. Yu, Ultrasound-Mediated Drug Delivery: Sonoporation Mechanisms, Biophysics, and Critical Factors, *BME Front.*, 2022, 9807347, DOI: 10.34133/2022/9807347.

17 E. McGraw, G. M. Laurent and A. Avila, Nanoparticle-Mediated Photoporation: Expanding Horizons in Drug Delivery, *Nanoscale Adv.*, 2024, **6**, 5007–5019, DOI: 10.1039/d4na00122b.

18 X. Du, M. Zhao, L. Jiang, L. Pang, J. Wang, Y. Lv, C. Yao and R. Wu, A Mini-Review on Gene Delivery Technique Using Nanoparticles-Mediated Photoporation Induced by Nanosecond Pulsed Laser, *Drug Delivery*, 2024, **31**(1), 2306231, DOI: 10.1080/10717544.2024.2306231.

19 J. M. Meacham, K. Durvasula, F. L. Degertekin and A. G. Fedorov, Physical Methods for Intracellular Delivery: Practical Aspects from Laboratory Use to Industrial-Scale Processing, *J. Lab. Autom.*, 2014, **19**(1), 1–18, DOI: 10.1177/2211068213494388.

20 Y.-C. Wu, T.-H. Wu, D. L. Clemens, B.-Y. Lee, X. Wen, M. A. Horwitz, M. A. Teitell and P.-Y. Chiou, Massively Parallel Delivery of Large Cargo into Mammalian Cells with Light Pulses, *Nat. Methods*, 2015, **12**(5), 439–444, DOI: 10.1038/nmeth.3357.

21 R. Xiong, D. Hua, J. Van Hoeck, D. Berdecka, L. Léger, S. De Munter, J. C. Fraire, L. Raes, A. Harizaj, F. Sauvage, G. Goetgeluk, M. Pille, J. Aalders, J. Belza, T. Van Acker, E. Bolea-Fernandez, T. Si, F. Vanhaecke, W. H. De Vos, B. Vandekerckhove, J. van Hengel, K. Raemdonck, C. Huang, S. C. De Smedt and K. Braeckmans, Photothermal Nanofibres Enable Safe Engineering of Therapeutic Cells, *Nat. Nanotechnol.*, 2021, **16**(11), 1281–1291, DOI: 10.1038/s41565-021-00976-3.

22 P. Shinde, S. Kar, M. Loganathan, H.-Y. Chang, F.-G. Tseng, M. Nagai and T. S. Santra, Infrared Pulse Laser-Activated Highly Efficient Intracellular Delivery Using Titanium Microdish Device, *ACS Biomater. Sci. Eng.*, 2020, **6**(10), 5645–5652, DOI: 10.1021/acsbiomaterials.0c00785.

23 H. G. Breunig, A. Uchugonova, A. Batista and K. König, Software-Aided Automatic Laser Optoporation and Transfection of Cells, *Sci. Rep.*, 2015, **5**, 11185, DOI: 10.1038/srep11185.

24 S. Kumar, A. Li, N. N. Thadhani and M. R. Prausnitz, Optimization of Intracellular Macromolecule Delivery by Nanoparticle-Mediated Photoporation, *Nanomedicine*, 2021, **37**, 102431, DOI: 10.1016/j.nano.2021.102431.

25 T. E. Pylaev, E. S. Avdeeva, B. N. Khlebtsov, M. V. Lomova and N. G. Khlebtsov, High-Throughput Cell Optoporation System Based on Au Nanoparticle Layers Mediated by Resonant Irradiation for Precise and Controllable Gene Delivery, *Sci. Rep.*, 2024, **14**, 3044, DOI: 10.1038/s41598-024-53126-9.

26 R. Xiong, K. Raemdonck, K. Peynshaert, I. Lentacker, I. De Cock, J. Demeester, S. C. De Smedt, A. G. Skirtach and K. Braeckmans, Comparison of Gold Nanoparticle Mediated Photoporation: Vapor Nanobubbles Outperform Direct Heating for Delivering Macromolecules in Live Cells, *ACS Nano*, 2014, **8**(6), 6288–6296, DOI: 10.1021/nn5017742.

27 A. Prasad, R. Gayathri, B. Nandhini., R. Jayaganthan, S. Kar and T. S. Santra, Microfluidic Synthesis of Iron Oxide Nanoparticles for Highly Efficient Intracellular Delivery in Stem Cells and Cancer Cells, *Lab Chip*, 2025, **25**(20), 5350–5366, DOI: 10.1039/d5lc00448a.
28 L. Wang, X. Wei, H. Liu and Y. Fan, Nanomaterial-Mediated Photoporation for Intracellular Delivery, *Acta Biomater.*, 2023, 24–48, DOI: 10.1016/j.actbio.2022.12.050.
29 R. Xiong, S. K. Samal, J. Demeester, A. G. Skirtach, S. C. De Smedt and K. Braeckmans, Laser-Assisted Photoporation: Fundamentals, Technological Advances and Applications, *Adv. Phys.: X*, 2016, 596–620, DOI: 10.1080/23746149.2016.1228476.
30 J. Ramon, R. Xiong, S. C. De Smedt, K. Raemdonck and K. Braeckmans, Vapor Nanobubble-Mediated Photoporation Constitutes a Versatile Intracellular Delivery Technology, *Curr. Opin. Colloid Interface Sci.*, 2021, 101453, DOI: 10.1016/j.cocis.2021.101453.
31 X. Du, J. Wang, Q. Zhou, L. Zhang, S. Wang, Z. Zhang and C. Yao, Advanced Physical Techniques for Gene Delivery Based on Membrane Perforation, *Drug Delivery*, 2018, **25**(1), 1516–1525, DOI: 10.1080/10717544.2018.1480674.
32 A. Harizaj, M. Wels, L. Raes, S. Stremersch, G. Goetgeluk, T. Brans, B. Vandekerckhove, F. Sauvage, S. C. De Smedt, I. Lentacker and K. Braeckmans, Photoporation with Biodegradable Polydopamine Nanosensitizers Enables Safe and Efficient Delivery of MRNA in Human T Cells, *Adv. Funct. Mater.*, 2021, **31**(28), 2102472, DOI: 10.1002/adfm.202102472.
33 M. Tsoli, H. Kuhn, W. Brandau, H. Esche and G. Schmid, Cellular Uptake and Toxicity of Au55 Clusters, *Small*, 2005, **1**(8–9), 841–844, DOI: 10.1002/smll.200500104.
34 M. Szwed, A. Poczta-Krawczyk, K. Bukowski and A. Marczak, Nanoparticle-Mediated Ferroptosis for Cancer Therapy: Mechanisms and Therapeutic Strategies, *Nanotechnol., Sci. Appl.*, 2025, **18**, 445–470, DOI: 10.2147/NSA.S550828.
35 E. Vanzha, T. Pylaev, A. Prilepskii, A. Golubev, B. Khlebtsov, V. Bogatyrev and N. Khlebtsov, Cell Culture Surfaces with Immobilized Gold Nanostars: A New Approach for Laser-Induced Plasmonic Cell Optoporation, *Proc. SPIE*, 2017, **10336**, 103360L, DOI: 10.1117/12.2269948.
36 T. S. Santra, *Microfluidics and Bio-MEMS: Devices and Applications*, Jenny Stanford Publishing, 1st edn, 2020.
37 Z. Lyu, F. Zhou, Q. Liu, H. Xue, Q. Yu and H. Chen, A Universal Platform for Macromolecular Deliveryinto Cells Using Gold Nanoparticle Layers via the Photoporation Effect, *Adv. Funct. Mater.*, 2016, **26**(32), 5787–5795, DOI: 10.1002/adfm.201602036.
38 A. Raun, N. Saklayen, C. Zgrabik, W. Shen, M. Madrid, M. Huber, E. Hu and E. Mazur, A Comparison of Inverted and Upright Laser-Activated Titanium Nitride Micropyramids for Intracellular Delivery, *Sci. Rep.*, 2018, **8**, 15595, DOI: 10.1038/s41598-018-33885-y.
39 C. Zhao, T. Man, X. Xu, Q. Yang, W. Liu, S. J. Jonas, M. A. Teitell, P. Y. Chiou and P. S. Weiss, Photothermal Intracellular Delivery Using Gold Nanodisk Arrays, *ACS Mater. Lett.*, 2020, **2**(11), 1475–1483, DOI: 10.1021/acsmaterialslett.0c00428.
40 A. T. Smith, A. M. LaChance, S. Zeng, B. Liu and L. Sun, Synthesis, Properties, and Applications of Graphene Oxide/Reduced Graphene Oxide and Their Nanocomposites, *Nano Mater. Sci.*, 2019, **1**(1), 31–47, DOI: 10.1016/j.nanoms.2019.02.004.
41 D. G. Papageorgiou, I. A. Kinloch and R. J. Young, Mechanical Properties of Graphene and Graphene-Based Nanocomposites, *Prog. Mater. Sci.*, 2017, **90**, 75–127, DOI: 10.1016/j.pmatsci.2017.07.004.
42 E. L. Wolf, Physical and Electrical Properties of Graphene, in *Applications of Graphene: An Overview*, ed. E. L. Wolf, Springer International Publishing, Cham, 2014, pp. 1–18, DOI: 10.1007/978-3-319-03946-6_1.
43 A. A. Balandin, Thermal Properties of Graphene and Nanostructured Carbon Materials, *Nat. Mater.*, 2011, **10**(8), 569–581, DOI: 10.1038/nmat3064.
44 F. Bonaccorso, Z. Sun, T. Hasan and A. C. Ferrari, Graphene Photonics and Optoelectronics, *Nat. Photonics*, 2010, **4**(9), 611–622, DOI: 10.1038/nphoton.2010.186.
45 M. K. Kavitha and M. Jaiswal, Graphene: A Review of Optical Properties and Photonic Applications, *Asian J. Phys.*, 2016, **25**, 809–831.
46 C. Liao, Y. Li and S. C. Tjong, Graphene Nanomaterials: Synthesis, Biocompatibility, and Cytotoxicity, *Int. J. Mol. Sci.*, 2018, **19**(11), 3564, DOI: 10.3390/ijms19113564.
47 S. H. Kang, Y. C. Shin, E. Y. Hwang, J. H. Lee, C.-S. Kim, Z. Lin, S. H. Hur, D.-W. Han and S. W. Hong, Engineered ''Coffee-Rings'' of Reduced Graphene Oxide as Ultrathin Contact Guidance to Enable Patterning of Living Cells, *Mater. Horiz.*, 2019, **6**(5), 1066–1079, DOI: 10.1039/C8MH01381K.
48 R. Y. N. Gengler, D. S. Badali, D. Zhang, K. Dimos, K. Spyrou, D. Gournis and R. J. D. Miller, Revealing the Ultrafast Process behind the Photoreduction of Graphene Oxide, *Nat. Commun.*, 2013, **4**(1), 2560, DOI: 10.1038/ncomms3560.
49 Abid, P. Sehrawat, S. S. Islam, P. Mishra and S. Ahmad, Reduced Graphene Oxide (RGO) Based Wideband Optical Sensor and the Role of Temperature, Defect States and Quantum Efficiency, *Sci. Rep.*, 2018, **8**, 3537, DOI: 10.1038/s41598-018-21686-2.
50 J. Liu, C. Li, T. Brans, A. Harizaj, S. Van de Steene, T. De Beer, S. De Smedt, S. Szunerits, R. Boukherroub, R. Xiong and K. Braeckmans, Surface Functionalization with Polyethylene Glycol and Polyethyleneimine Improves the Performance of Graphene-based Materials for Safe and Efficient Intracellular Delivery by Laser-Induced Photoporation, *Int. J. Mol. Sci.*, 2020, **21**(4), 1540, DOI: 10.3390/ijms21041540.
51 Z. Li, H. Lei, A. Kan, H. Xie and W. Yu, Photothermal Applications Based on Graphene and Its Derivatives: A State-of-the-Art Review, *Energy*, 2021, **216**, DOI: 10.1016/j.energy.2020.119262.
52 H. H. Padma, K. Illath, D. Dominic, H.-Y. Chang, M. Nagai, R. Ojha, S. Kar and T. S. Santra, Ultra-Low Intensity Light Pulses for Large Cargo Delivery into Hard-to-Transfect Cells Using an RGO Mixed PDMS Microtip Device, *Lab Chip*, 2024, **24**(16), 3880–3897, DOI: 10.1039/D4LC00121D.

53 H. H. Padma, D. Dominic, K. Illath, S. Kar and T. S. Santra, Light-Activated Nanocomposite Thin Sheet for High Throughput Contactless Biomolecular Delivery into Hard-to-Transfect Cells, *Analyst*, 2025, **150**, 860–876, DOI: 10.1039/d4an01331j.
54 D. C. Marcano, D. V. Kosynkin, J. M. Berlin, A. Sinitskii, Z. Sun, A. Slesarev, L. B. Alemany, W. Lu and J. M. Tour, Improved Synthesis of Graphene Oxide, *ACS Nano*, 2010, **4**(8), 4806–4814, DOI: 10.1021/nn1006368.
55 D. C. Marcano, D. V. Kosynkin, J. M. Berlin, A. Sinitskii, Z. Sun, A. S. Slesarev, L. B. Alemany, W. Lu and J. M. Tour, Correction to Improved Synthesis of Graphene Oxide, *ACS Nano*, 2018, **12**(2), 2078, DOI: 10.1021/acsnano.8b00128.
56 W. S. Hummers, Jr. and R. E. Offeman, Preparation of Graphitic Oxide, *J. Am. Chem. Soc.*, 1958, **80**(6), 1339, DOI: 10.1021/ja01539a017.
57 N. I. Zaaba, K. L. Foo, U. Hashim, S. J. Tan, W.-W. Liu and C. H. Voon, Synthesis of Graphene Oxide Using Modified Hummers Method: Solvent Influence, *Proc. Eng.*, 2017, **184**, 469–477, DOI: 10.1016/j.proeng.2017.04.118.
58 D. Li, W. Zhang, X. Yu, Z. Wang, Z. Su and G. Wei, When Biomolecules Meet Graphene: From Molecular Level Interactions to Material Design and Applications, *Nanoscale*, 2016, 19491–19509, DOI: 10.1039/c6nr07249f.
59 B. S. Dash, G. Jose, Y. J. Lu and J. P. Chen, Functionalized Reduced Graphene Oxide as a Versatile Tool for Cancer Therapy, *Int. J. Mol. Sci.*, 2021, 1–24, DOI: 10.3390/ijms22062989.
60 M. Soni, P. Kumar, R. Kumar, S. K. Sharma and A. Soni, Photo-Catalytic Reduction of Oxygenated Graphene Dispersions for Supercapacitor Applications, *J. Phys. D: Appl. Phys.*, 2017, **50**(12), 124003, DOI: 10.1088/1361-6463/aa5c9f.
61 M. Layachi, A. Treizebré, L. Hay, D. Gilbert, J. Pesez, Q. D'Acremont, K. Braeckmans, Q. Thommen and E. Courtade, Novel Opto-Fluidic Drug Delivery System for Efficient Cellular Transfection, *J. Nanobiotechnol.*, 2023, **21**(1), 43, DOI: 10.1186/s12951-023-01797-3.
62 G. Rajeswari, S. Kar, M. Nagai, P. S. Mahapatra and T. S. Santra, Massively Parallel High-Throughput Single-Cell Patterning and Large Biomolecular Delivery in Mammalian Cells Using Light Pulses, *Small*, 2023, **19**(47), e2303053, DOI: 10.1002/smll.202303053.
63 B. Hu, L. Zhong, Y. Weng, L. Peng, Y. Huang, Y. Zhao and X.-J. Liang, Therapeutic SiRNA: State of the Art, *Signal Transduction Targeted Ther.*, 2020, **5**(1), 101, DOI: 10.1038/s41392-020-0207-x.
64 H. Dana, G. M. Chalbatani, H. Mahmoodzadeh, R. Karimloo, O. Rezaiean, A. Moradzadeh, N. Mehmandoost, F. Moazzen, A. Mazraeh, V. Marmari, M. Ebrahimi, M. M. Rashno, S. J. Abadi and E. Gharagouzlo, Molecular Mechanisms and Biological Functions of SiRNA, *Int. J. Biomed. Sci.*, 2017, **13**(2), 48–57.
65 M. Kranjc, S. Kranjc Brezar, G. Serša and D. Miklavčič, Contactless Delivery of Plasmid Encoding EGFP in Vivo by High-Intensity Pulsed Electromagnetic Field, *Bioelectrochemistry*, 2021, **141**, 107847, DOI: 10.1016/j.bioelechem.2021.107847.
66 A. C. Ferrari and J. Robertson, Interpretation of Raman Spectra of Disordered and Amorphous Carbon, *Phys. Rev. B: Condens. Matter Mater. Phys.*, 2000, **61**(20), 14095–14107, DOI: 10.1103/PhysRevB.61.14095.
67 W. Gao, P. Xiao, G. Henkelman, K. M. Liechti and R. Huang, Interfacial Adhesion between Graphene and Silicon Dioxide by Density Functional Theory with van der Waals Corrections, *J. Phys. D: Appl. Phys.*, 2014, **47**(25), 255301, DOI: 10.1088/0022-3727/47/25/255301.
68 S. P. Koenig, N. G. Boddeti, M. L. Dunn and J. S. Bunch, Ultrastrong Adhesion of Graphene Membranes, *Nat. Nanotechnol.*, 2011, **6**(9), 543–546, DOI: 10.1038/nnano.2011.123.
69 M. Massicotte, G. Soavi, A. Principi and K. J. Tielrooij, Hot Carriers in Graphene-Fundamentals and Applications, *Nanoscale*, 2021, 8376–8411, DOI: 10.1039/d0nr09166a.
70 S. Kar, D. Mohapatra, F. Eric and A. Sood, Tuning Photo-induced Terahertz Conductivity in Monolayer Graphene: Optical Pump Terahertz Probe Spectroscopy, *Phys. Rev. B: Condens. Matter Mater. Phys.*, 2014, **90**(16), 165420, DOI: 10.1103/PhysRevB.90.165420.
71 S. Kar, V. L. Nguyen, D. R. Mohapatra, Y. H. Lee and A. K. Sood, Ultrafast Spectral Photoresponse of Bilayer Graphene: Optical Pump-Terahertz Probe Spectroscopy, *ACS Nano*, 2018, **12**(2), 1785–1792, DOI: 10.1021/acsnano.7b08555.
72 J. Liu, P. Li, S. Xu, Y. Xie, Q. Wang and L. Ma, Temperature Dependence of Thermal Conductivity of Giant-Scale Supported Monolayer Graphene, *Nanomaterials*, 2022, **12**(16), 2799, DOI: 10.3390/nano12162799.
73 E. Pop, V. Varshney and A. K. Roy, Thermal Properties of Graphene: Fundamentals and Applications, *MRS Bull.*, 2012, **37**(12), 1273–1281, DOI: 10.1557/mrs.2012.203.
74 K. F. Mak, C. H. Lui and T. F. Heinz, Measurement of the Thermal Conductance of the Graphene/SiO_2 Interface, *Appl. Phys. Lett.*, 2010, **97**(22), 221904, DOI: 10.1063/1.3511537.
75 S. Chen, M. Yang, B. Liu, M. Xu, T. Zhang, B. Zhuang, D. Ding, X. Huai and H. Zhang, Enhanced Thermal Conductance at the Graphene-Water Interface Based on Functionalized Alkane Chains, *RSC Adv.*, 2019, **9**(8), 4563–4570, DOI: 10.1039/C8RA09879D.
76 J. P. Layfield and D. Troya, Theoretical Study of the Dynamics of H + Alkane Reactions, *Chem. Phys. Lett.*, 2009, **467**(4–6), 243–248, DOI: 10.1016/j.cplett.2008.11.047.
77 Y. Xu, J. Jiang, B. Yang, M. Li, S. Xu and Y. Yue, Comparison of Thermal Conductance of Graphene/SiO_2 and Graphene/Au Interfaces Based on Raman Optothermal Method, *Mater. Res. Express*, 2019, **6**(11), DOI: 10.1088/2053-1591/ab4492.
78 T. S. Santra, S. Kar, T.-C. Chen, C.-W. Chen, J. Borana, M.-C. Lee and F.-G. Tseng, Near-Infrared Nanosecond-Pulsed Laser-Activated Highly Efficient Intracellular Delivery Mediated by Nano-Corrugated Mushroom-Shaped Gold-Coated Polystyrene Nanoparticles, *Nanoscale*, 2020, **12**(22), 12057–12067, DOI: 10.1039/D0NR01792B.